Supporting Information

Molecular Engineering of Pyridinium-Functionalized Metal-Organic Cages for Iodine Capture in Multiple Phase Media

Wen-Jun Chen,[a,b] Hua-Rong Shangguan,[a,c] Yi-Xin Wei,[a] Zhenqiang Wang,[d] and Feng-Rong Dai*[a,b]

[a] *State Key Laboratory of Structural Chemistry, Fujian Institute of Research on the Structure of Matter, Chinese Academy of Sciences, Fuzhou, Fujian 350002, China*

[b] *University of Chinese Academy of Sciences, Beijing, 100039, China*

[c] *Fujian College, University of Chinese Academy of Sciences, Fuzhou, 350002, China*

[d] *Department of Chemistry & Center for Fluorinated Functional Materials, University of South Dakota, Vermillion, SD, USA*

* Corresponding authors. E−mails: dfr@fjirsm.ac.cn

Experimental Procedures

General Methods: Powder X-ray diffraction (PXRD) patterns were acquired on a Rigaku Miniflex 600 diffractometer with Cu *Kα* radiation (λ = 1.54184 Å) over a 2θ range of 5-35 ° at room temperature with a scanning rate of 3 ° min^{-1}. X-ray photoelectron spectroscopy (XPS) was performed on a VG ESCALAB 250XI spectrometer. Nuclear magnetic resonance (NMR) spectra were obtained using a Bruker AVANCE III 400 MHz spectrometer. Fourier Transform Infrared (FT-IR) spectra were collected on a Bruker VERTEX 70 spectrometer. Raman spectra were recorded on a HORIBA Labram spectrometer. Scanning electron microscopy (SEM) images and energy−dispersive X-ray spectroscopy (EDS) analyses were obtained using a Nova Nano-SEM 450 microscope. Ultraviolet-visible (UV-Vis) absorption spectra were measured on a Perkin Elmer LAMBDA 365 spectrophotometer. Thermogravimetric analysis (TGA) was conducted on a Netzsch STA449F3 thermal analyzer at a heating rate of 10 ℃ min^{-1}. N_2 adsorption-desorption isotherms were collected at 77 K using a Micromeritics ASAP 2460 analyzer.

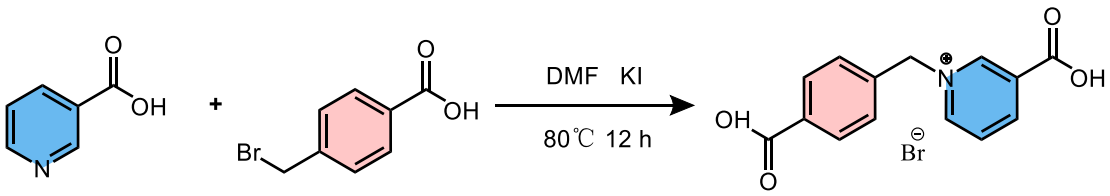

Synthesis of H_2**L3**: *p*-Bromomethylbenzoic acid (2.15 g, 10.00 mmol), isonicotinic acid (1.23 g, 10.00 mmol), and potassium iodide (83.00 mg, 0.50 mmol) were sequentially added to N,N-dimethylformamide (DMF, 10 mL). The resulting mixture was stirred at 80 ℃ for 12 h, then cooled to room temperature. Dichloromethane (DCM, 100 mL) was added, and the mixture was stirred for an additional 30 min to ensure thorough dispersion, leading to the formation of precipitation. The solid was collected by filtration, washed with diethyl ether (5 × 20 mL) to remove residual impurities and solvents, and subsequently dried under vacuum at 85 ℃ for 4 h. The target product was obtained as a white powder in 87.9% yield (2.98 g). ^{1}H NMR (400 MHz, DMSO-d_6): δ = 9.74 (s, 1H), 9.36 (dt, *J* = 6.1, 1.5 Hz, 1H), 8.99 (dt, *J* = 8.2, 1.6 Hz, 1H), 8.29 (td, *J* = 7.0, 1.6 Hz, 1H), 7.99 (dd, *J* = 8.3, 1.7 Hz, 2H), 7.66 (dd, *J* = 8.4, 1.7 Hz, 2H), 6.08 (s, 2H). ^{13}C NMR (100 MHz, DMSO-d_6): δ = 166.73, 162.96, 147.58, 146.26, 145.85, 138.54, 132.00, 131.56, 129.98, 129.00, 128.74, 62.78.

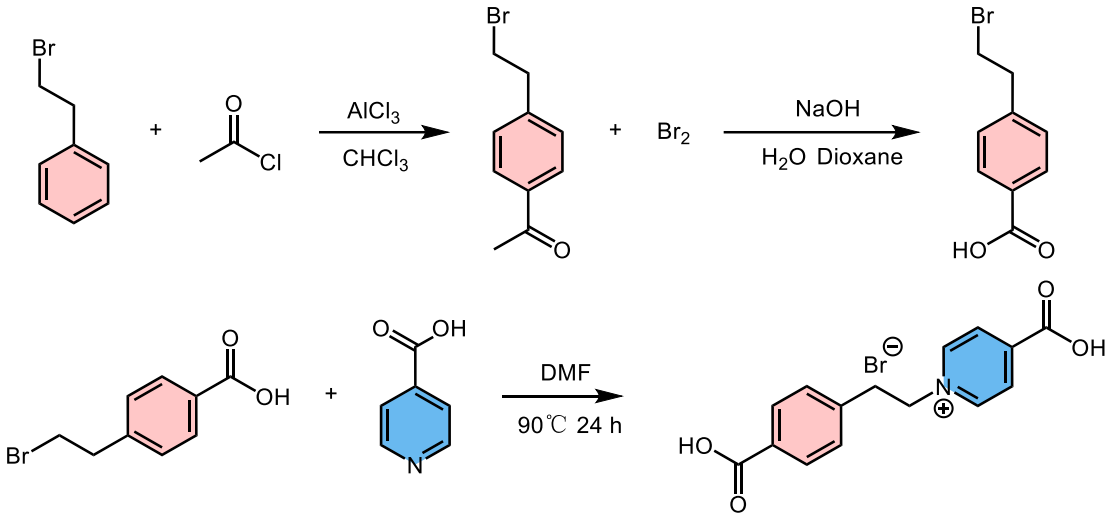

Synthesis of H_2**L4**: Anhydrous aluminum chloride (7.40 g, 54.00 mmol) and acetyl chloride (5.50 g, 70.00 mmol) were placed in a 200 mL Schlenk flask, and the mixture was stirred in chloroform (50 mL) at −10 ℃ for 30 min. 1-Bromoethylbenzene (11.10 g, 60.00 mmol) was then added dropwise, followed by the slow addition of another portion of acetyl chloride (4.71 g, 60 mmol). The reaction was stirred at −10 ℃ for 3 h. Subsequently, concentrated hydrochloric acid (6 M, 60 mL) was added dropwise at low temperature, and the mixture was allowed to warm to room temperature and stirred overnight under a nitrogen atmosphere. The resulting mixture was then allowed to stand for 10 min to separate the aqueous and organic phases. The aqueous phase was extracted with DCM (3 × 30 mL), and the combined organic phases were washed with deionized water (2 × 50 mL) and brine (3 × 50 mL), then dried over anhydrous sodium sulfate (Na_2SO_4). After filtration, the solvent was removed under reduced pressure at 45 ℃ to afford the crude product of 4-(2-bromoethyl) acetophenone as a pale yellow oil (12.20 g).

The crude product obtained from the previous step was used without further purification. A portion of this crude material (8.00 g) was transferred to a 500 mL Schlenk flask cooled to −10 ℃. 1,4-Dioxane (70 mL) , water (50 mL), and sodium hydroxide (NaOH, 11.80 g) were added sequentially, and the mixture was stirred for 30 min. A solution of bromine (Br_2, 17.20 g) in water (50 mL) was then added dropwise via a constant-pressure dropping funnel, and the reaction was stirred at −10 ℃ for an additional 4 h. Subsequently, concentrated hydrochloric acid (12 M, 24 mL) was carefully added, and the mixture was allowed to warm to room temperature and stirred overnight. The solvents (1,4-dioxane and residual water) were removed under reduced pressure at 75 ℃. The resulting residue was collected by filtration, washed with dilute hydrochloric acid (1 M), and dried. The dried solid was recrystallized from a small

amount of chloroform. The resulting crystals were collected by filtration and dried in vacuo to afford 4-(2-bromoethyl)benzoic acid as white flaky crystals (4.50 g, 55.8% yield over two steps). ^{1}H NMR (400 MHz, DMSO-d_6): δ = 12.89 (s, 1H), 7.88 (d, J = 7.8 Hz, 2H), 7.41 (d, J = 7.8 Hz, 2H), 3.77 (t, J = 7.0 Hz, 2H), 3.20 (t, J = 7.0 Hz, 2H). ^{13}C NMR (100 MHz, DMSO-d_6): δ = 167.68, 144.56, 129.85, 129.65, 129.42, 38.55, 34.39.

4-(2-Bromoethyl)benzoic acid (1.15 g, 5.00 mmol), isonicotinic acid (0.63 g, 5.10 mmol), and potassium iodide (42.00 mg, 0.25 mmol) were charged into a 250 mL two-necked flask. The flask was evacuated and backfilled with N_2 three times, after which anhydrous DMF (10 mL) was added. The reaction mixture was stirred at 90 ℃ for 24 h, then cooled to room temperature. Dichloromethane (100 mL) and diethyl ether (20 mL) were added to precipitate the product. The resulting solid was collected by filtration, washed with diethyl ether (3 × 10 mL), and dried under vacuum at 85 ℃ for 4 h. The target product of H_2**L4** was obtained as a yellow powder (1.71 g, 96.3% yield). ^{1}H NMR (400 MHz, DMSO-d_6): δ = 13.03 (s, 2H), 9.12 (d, J = 6.1 Hz, 2H), 8.40 (d, J = 6.0 Hz, 2H), 7.88 (d, J = 7.7 Hz, 2H), 7.36 (d, J = 7.8 Hz, 2H), 4.96 (t, J = 7.4 Hz, 2H), 3.37 (t, J = 7.4 Hz, 2H). ^{13}C NMR (100 MHz, DMSO-d_6): δ = 167.06, 163.52, 145.81, 141.24, 129.64, 129.19, 127.02, 61.16, 36.36.

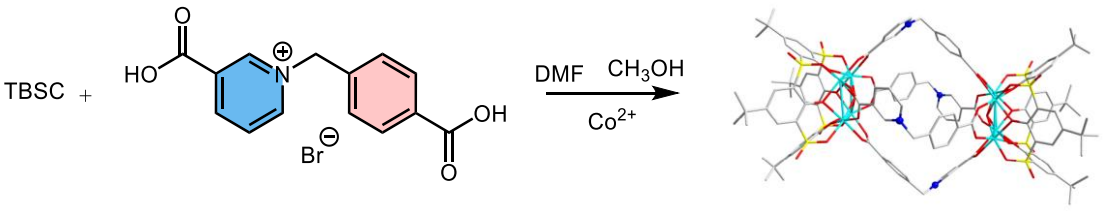

Synthesis of [Co_4(TBSC)(μ$_4$-OH)]$_2$(L3)$_4$(NO_3)$_2$ (Co-L3): Sulfonylcalix[4]arene (TBSC, 0.085 g, 0.10 mmol), cobalt (II) nitrate hexahydrate (0.16 g, 0.55 mmol) and H_2**L3** (0.073 g, 0.22 mmol) were dissolved in 2.5 mL of DMF under sonication for 10 min. The resulting clear solution was transferred to a 20 mL glass vial, heated to 100 ℃ over 140 min, and maintained at that temperature for 24 h in a sand bath. After slowly cooling to 25 ℃ over 500 min, the resulting solid was collected by filtration, rinsed with DMF, and then soaked in acetone for 12 h, during which the acetone was refreshed four times. Finally, the product was thermally activated under vacuum at 120 ℃ to afford **Co-L3** (0.12 g, 75.3% yield).

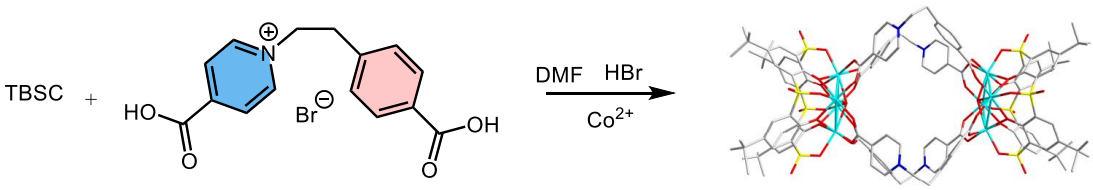

Synthesis of $[Co_4(TBSC)(\mu_4\text{-}OH)]_2(L4)_4Br_2$ (Co-L4): Sulfonylcalix [4] arene (TBSC, 0.085 g, 0.10 mmol), cobalt (II) nitrate hexahydrate (0.16 g, 0.55 mmol) and H_2**L4** (0.073 g, 0.22 mmol) were dissolved in DMF (2.5 mL) under sonication for 10 min, followed by the addition of HBr (5 μL). The resulting mixture was transferred to a 20 mL glass vial, heated to 100 ℃ over 140 min, and maintained at 100 ℃ for 24 h in a sand bath. After slowly cooling to 25 ℃ over 500 min, the resulting solid was collected by filtration, rinsed with DMF, and then soaked in acetone for 12 h, during which the acetone was refreshed four times. Finally, the product was thermally activated under vacuum at 120 ℃ to afford **Co-L4** (0.11 g, 70.0% yield).

X-Ray Crystallography: Single-crystal X-ray diffraction data for **Co-L3** were acquired at 100 K on a Rigaku Synergy-R-Mo diffractometer with Mo-Kα radiation (λ = 0.71073 Å). Meanwhile, the single-crystal XRD test of **Co-L4** was carried out at 298 K using a Rigaku Synergy-R-Ga diffractometer and Ga-Kα radiation (λ = 1.34140 Å). The CrystalClear or CrysAlisPro software package was used for data reduction and empirical absorption correction. The crystal structures were solved by the SHELXT method implemented in the Olex2 program, and the full-matrix least-squares refinement on F^2 was carried out using the SHELXT program. All non-hydrogen atoms were refined with anisotropic displacement parameters. Hydrogen atoms were positioned geometrically and assigned fixed isotropic displacement parameters.

Iodine Vapor Adsorption: Gravimetric iodine vapor adsorption experiments were conducted at 75 ℃ using a sealed static adsorption system. Three sample vials were prepared: one containing I_2 (3.00 g), an empty vial as a blank, and one vials containing the activated adsorbents (**Co-L1**, **Co-L2**, **Co-L3**, or **Co-L4**). These vials were placed together in a transparent glass jar (40 × 70 mm), which was then sealed and immersed in a sand bath inside a preheated constant-temperature blast drying oven to ensure uniform heating. The temperature was maintained at 75 ℃ throughout the experiment. At predetermined time intervals, the sample vials were removed, quickly weighed, and immediately returned to the sealed glass jar. The iodine uptake at time t (q_t, mg g^{-1}) was calculated based on the mass increase of the sample.

$$q_t = \frac{(m_t - m_{0,g}) - (m_{e,t} - m_{e,0})}{m_{0,g} - m_0}$$

q_t denotes the I_2 vapor adsorption capacity of the adsorbent at time t; m_t is the mass of the sample vial at time t; m_0 represents the mass of the empty sample vial before the addition of the adsorbent; $m_{0,g}$ refers to the mass of the sample vial at the start of the test; $m_{e,0}$ is the mass of the blank sample vial at time 0; and $m_{e,t}$ denotes the mass of the blank sample vial at time t.

Iodine Adsorption from n-Hexane Solution: An iodine (I_2) stock solution (1 mM in n-hexane) was prepared. Activated adsorbent (20.00 mg, **Co-L1**, **Co-L2**, **Co-L3**, or **Co-L4**) was weighed and immersed in the I_2 solution (20 mL). At predetermined time intervals, an aliquot of the solution was withdrawn, filtered through a 0.22 μm organic membrane, and its UV-Vis absorbance was measured immediately.

Aqueous I_3^- Adsorption and Recycling Experiments: A stock solution of I_3^- (0.15~0.4 mM) was prepared by dissolving KI and I_2 in deionized water at a molar ratio of 5 : 1. Activated adsorbent (20.00 mg, **Co-L1**, **Co-L2**, **Co-L3**, or **Co-L4**) was weighed and dispersed in the I_3^- solution (200 mL). At predetermined time intervals, an aliquot of the suspension was withdrawn, filtered through a 0.22 μm aqueous membrane, and its UV-Vis absorbance was measured immediately.

For cycling experiments, the adsorbent (100 mg) was subjected to iodine adsorption under the same conditions. After adsorption, the solid was collected by centrifugation, immersed in a mixture of ethanol and $Na_2S_2O_3$ solution for 12 h to desorb iodine, during which the desorption solvent was refreshed four times. The regenerated adsorbent was dried under vacuum at 120 ℃ for 4 h, characterized by PXRD, and then reused in subsequent adsorption cycles.

Dynamic Flow-Through Aqueous I_3^- Adsorption: A stock solution of I_3^- (0.06 mM, 1 L) was prepared by dissolving KI and I_2 in deionized water at a molar ratio of 5 : 1, and continuously delivered using a peristaltic pump. Activated **Co-L4** (25.00 mg) was packed into the pipeline, and the I_3^- solution was repeatedly circulated through the adsorbent. After each complete passage of the solution, an aliquot of the effluent was collected to measure its UV-Vis absorbance. The flow rate was maintained at 20 mL min^{-1} throughout the experiment.

For ion competition studies, potassium bicarbonate ($KHCO_3$), potassium nitrate (KNO_3), potassium chloride (KCl), Potassium Bromide (KBr) and potassium sulfate (K_2SO_4) were selected as competing salts. The concentration of each competing anion was set to ten times that of I_3^-. The UV-Vis absorbance of the solution after two cycles was measured and compared with that of a control group containing no competing ions.

Kinetic Calculations: To investigate the adsorption kinetic characteristics, the *pseudo*-first-order (PFO) and *pseudo*-second-order (PSO) kinetic models were adopted:
Pseudo-first-order kinetic model:

$$q_t = q_e(1\text{-}e^{-tk_1})$$

Pseudo−second−order kinetic model:

$$q_t = \frac{tk_2q_e^2}{1+tk_2q_e}$$

q_t (mg g^{-1}) and q_e (mg g^{-1}) represent the adsorption capacity at adsorption time t (min) and the equilibrium adsorption capacity, respectively; k_1 (min^{-1}) and k_2 (g mg^{-1} min^{-1}) denote the adsorption rate constants for the *pseudo*-first-order and *pseudo*-second-order kinetic models, respectively.

Weber-Morris Intraparticle Diffusion Model: To further explore the adsorption diffusion mechanism, the Weber-Morris intraparticle diffusion model was employed:

Weber-Morris intraparticle diffusion model:

$$q_t = k_{id}t^{1/2}+C$$

q_t (mg g^{-1}) is the adsorption capacity at adsorption time t (min); k_{id} (mg g^{-1} $min^{-1/2}$) is the intraparticle diffusion rate constant; C (mg g^{-1}) is the boundary layer thickness constant, which reflects the effect of the boundary layer on adsorption. A larger value of C indicates a stronger influence of the boundary layer.

Thermodynamic Calculations: To explore the adsorption isotherm characteristics, the *Langmuir* and *Freundlich* isotherm models were adopted:
Langmuir isotherm model:

$$q_e = \frac{q_mK_LC_e}{1+K_LC_e}$$

Freundlich isotherm model:

$$q_e = K_F C_e^{1/n}$$

qe (mg g^{-1}) and qm (mg g^{-1}) represent the equilibrium adsorption capacity and the theoretical maximum monolayer adsorption capacity, respectively; *Ce* (mg L^{-1}) is the equilibrium concentration of adsorbate in solution; K_L (L mg^{-1}) is the Langmuir adsorption constant; K_F (mg g^{-1} (L mg^{-1})1/n) and n are the Freundlich constant and heterogeneity factor, respectively.

DFT calculation method

The theoretical calculations were implemented by using Gaussian 16 program package[1] with density functional theory (DFT) method at the B3LYP level[2-3] adding the D3 version of Grimme's dispersion with the original D3 damping function[4] for these metal-organic cages (MOCs) **Co-Ln** (n = 1-4). The Stuttgart-Dresden (SDD) basis set and the effective core potentials (ECPs)[5] were used to describe the Co atoms, while other non-metal atoms of S, O, N, C and H were described by the all-electron basis set of 6-31G**. Considering the number of unpaired electrons in the outer shell of Ni atoms, the spin multiplicity of these MOCs containing 8 Co atoms is set to 25. The electrostatic potential (ESP) distribution of **Co-Ln** (n = 1-4) was employed to evaluate the charge distribution of the MOCs and performed by GaussView.

Table S1. Crystallographic Data for **Co-L3** and **Co-L4**.

	Co-L3	**Co-L4**
Empirical formula	$C_{175}H_{219}Co_8N_{19}O_{61}S_8$	$C_{140}H_{132}Co_8N_4O_{42}S_8Br_2$
Formula weight	4292.60	3430.23
Temperature (K)	100	293
Wavelength	0.71073	1.34139
Crystal system	Triclinic	Triclinic
space group	$P\bar{1}$	$P\bar{1}$
a (Å)	11.9825	14.2344
b (Å)	16.3751	14.5125
c (Å)	26.5156	26.3271
α (°)	103.689	98.104
β (°)	94.326	98.975
γ (°)	100.949	98.098
V (Å^3)	4923.26	5244.06
Z	1	1
D (calcd) (g cm^{-3})	1.448	1.086
μ (mm^{-1})	0.830	4.492
F (000)	2234	1750
Reflections collected	71940	65905
Independent reflections	24814 [R_{int}=0.0387]	19828 [R_{int}=0.0438]
Data/ restraints/ parameters	24814/931/1441	19828/518/103
GOF	1.041	1.028
R_1 ($I>2\sigma(I)$)	0.0897	0.1007
wR_2 ($I>2\sigma(I)$)	0.2301	0.2360
R_1 (all data)	0.1252	0.1592
wR_2 (all data)	0.2512	0.2645
$\Delta\rho$/e Å^{-3}	1.79, −1.07	1.71, −00.39
Limiting indices	−14≤h≤16 −22≤k≤23 −37≤l≤33	−16≤h≤16 −17≤k≤12 −31≤l≤30

Table S2. Comparison of I_3^- adsorption capacities with previously reported materials.

Type	Materials	Adsorption ($g\ g^{-1}$)	Time	Ref.
Molecular sieve	Ag-SBA-15	0.38	20 h	[6]
Molecular sieve	Ag @ZnAl-LDH	0.256	6 days	[7]
Silica foam	MSF@PEI-Im	1.215	—	[8]
Microsphere	P[VBIm]PTC-2	0.679	7 h	[9]
Zeolite	EMM-17	0.42	4 h	[10]
Zeolite	Cu @FSL-1	0.625	45 min	[11]
POPs	TU-POP-1	1.731	24 h	[12]
POPs	Ag-MSHC	0.77	2 h	[13]
POPs	MBM	0.88	30 min	[14]
POPs	HCP[$H_{200}P_3$]	0.92	2h	[15]
POPs	Compound-1(TPT-3Im)	1.21	30 min	[16]
POPs	P5-P5I	0.942	15 min	[17]
MOFs	{[Co_2(DPT)$_2$(HTATB)$_2$] 0.5 H_2O 3.75DMA}$_n$	1.97	12 h	[18]
MOFs	$Cu_3HOCl_2(TRZ)_3$	1.246	200 min	[19]
MOFs	Co-tib	2.3	—	[20]
MOFs	MC_2	2.26	48 h	[21]
MOFs	1-NTf_2	1.1	70 min	[22]
MOFs	H_2oxdz	0.816	48 h	[23]
MOFs	ALP-MOF-2	1.5	5 h	[24]
MOFs	CN-223-HPP	1.2	10 h	[25]
MOFs	{[Mn_2(oxdz)$_2$(tpbn)(H2O)$_2$] · $2C_2H_5OH$}$_n$	1.1	36 h	[26]
MOFs	NH2-MOF	0.94	10 h	[27]
MOFs	Zn(ttr)(OAc)	0.846	11 h	[28]
COFs	COF-DtATH	0.337	150 min	[29]
COFs	H_COF-1	2.1	240 min	[30]
COFs	H_COF-7	1.39	6 h	[31]
COFs	BOF-1	0.93	10 h	[32]

COFs	HOF-TAM–BDA	1.12	1 h	[33]
COFs	TAPB-BPDA	0.988	90 min	[34]
COFs	OH-ExR$_4$	0.625	—	[35]
COFs	Fe_3O_4/COF	0.797	—	[36]
COFs	BTPA-TTA COF	4.22	24 h	[37]
MOCs	3 6Br ($C_{54}H_{48}N_{12}$ 6Br)	1.10	—	[38]
MOCs	$[M_8L_4]_8^+$	0.83	24 h	[39]
MOCs	PyrC	1.97	45 min	[40]
MOCs	MS-Cu_x-Zr_y	0.23	—	[41]
MOCs	$[Zn_4(TPBA)_4(ClO4)_8]$	0.144	450 min	[42]
MOCs	**Co-L2**	0.941	3 h	This work.
MOCs	**Co-L3**	1.25	3 h	This work.
MOCs	**Co-L4**	1.34	3 h	This work.

Table S3. Capacity of I_2 adsorption in vapor.

Sample	**Co-L1**	**Co-L2**	**Co-L3**	**Co-L4**
medium		I_2 Vapor		
$Q_{t,1}$ (mg g^{-1})	350.8	428.5	440.2	650.5
Time	24h	24h	24h	24h
		Pseudo-first-order		
k_1 (min^{-1})	3.70×10^{-2}	1.87×10^{-2}	2.09×10^{-2}	6×10^{-2}
R^2	0.933	0.975	0.997	0.995
		Pseudo-second-order		
Qe (mg g^{-1})	355.8	440.5	454.5	653.5
k_2 (g mg^{-1} min^{-1})	2.71×10^{-4}	2.17×10^{-4}	3.08×10^{-4}	6.72×10^{-4}
R^2	0.9986	0.9991	0.9960	0.9995
$Q_{t,2}$, under humid conditions	304.5	374.3	399.6	621.3

Table S4. Capacity of I_3^- Adsorption in KI/I_2=5:1 aqueous.

Sample	**Co-L1**	**Co-L2**	**Co-L3**	**Co-L4**
medium		KI/I_2 = 5:1 Aqueous		
Capacity (mg g^{-1})	243.5	941.5	1253.0	1345.2
Time	3h	3h	3h	3h
		Pseudo-first-order		
k_1 (min^{-1})	0.139	7.41×10^{-2}	3.97×10^{-2}	2.88×10^{-2}
R^2	0.957	0.889	0.877	0.950
		Pseudo-second-order		
*Q*e (mg g^{-1})	250.0	990.1	1344.06	1545.6
k_2 (g mg^{-1} min^{-1})	8.41×10^{-4}	9.10×10^{-5}	4.88×10^{-5}	2.34×10^{-5}
R^2	0.9992	0.9974	0.9982	0.9838

Table S5. Langmuir and Freundlich isothermal adsorption model fitting.

Sample	**Co-L1**	**Co-L2**	**Co-L3**	**Co-L4**
		Langmiur isotherm		
Q_m	279.4	993.4	1376.1	1423.5
K_L	0.053	0.140	0.157	0.293
R^2	0.9981	0.9940	0.9887	0.9866
		Freudlich isotherm		
K_F	57.8	303	311.0	440.5
n	1.422	2.201	2.641	3.077
R^2	0.7709	0.8677	0.9391	0.9253

Table S6. DFT pore size distribution and pore region characteristics.

Sample	Most probable pore size (nm)	dV/dw	Main pore region
Co-L1	2.63	0.0116	Micropore/small mesopore
Co-L2	2.51	0.0191	Ultramicropore
Co-L3	9.90/8.31	0.0078	Hierarchically dispersed
Co-L4	12.93/2.63	0.0133/0.0103	Mesopore/micropore

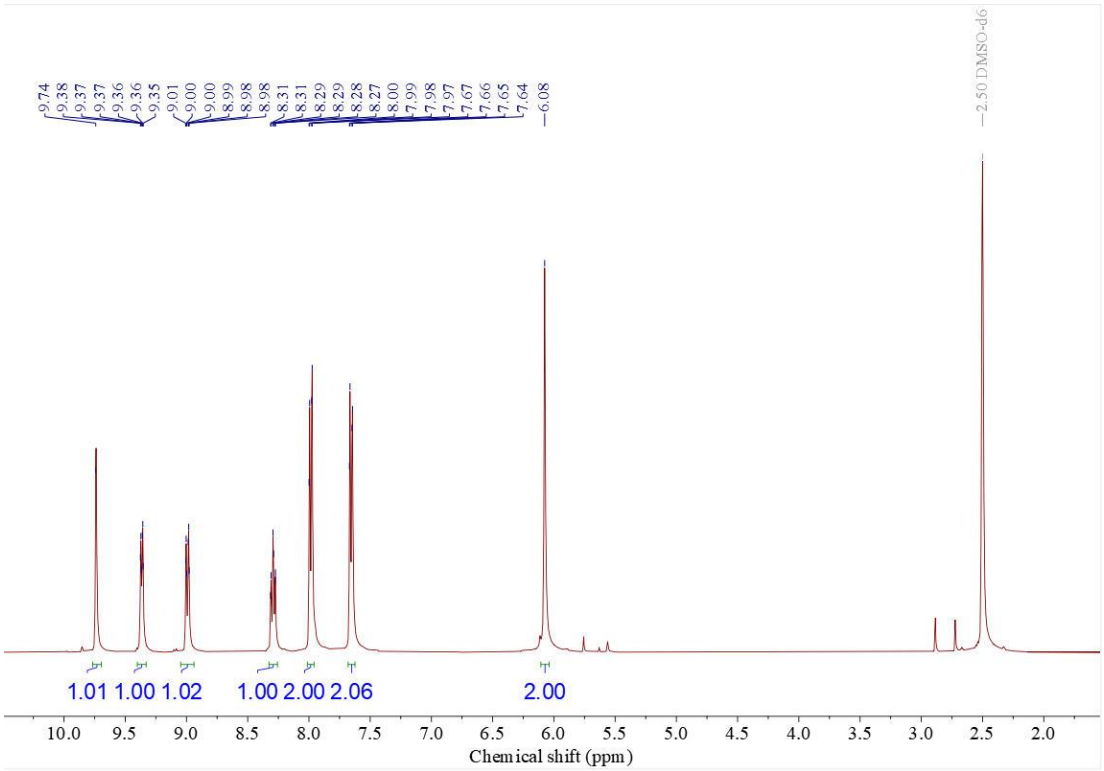

Figure S1. ^{1}H NMR spectrum of H_2**L3**.

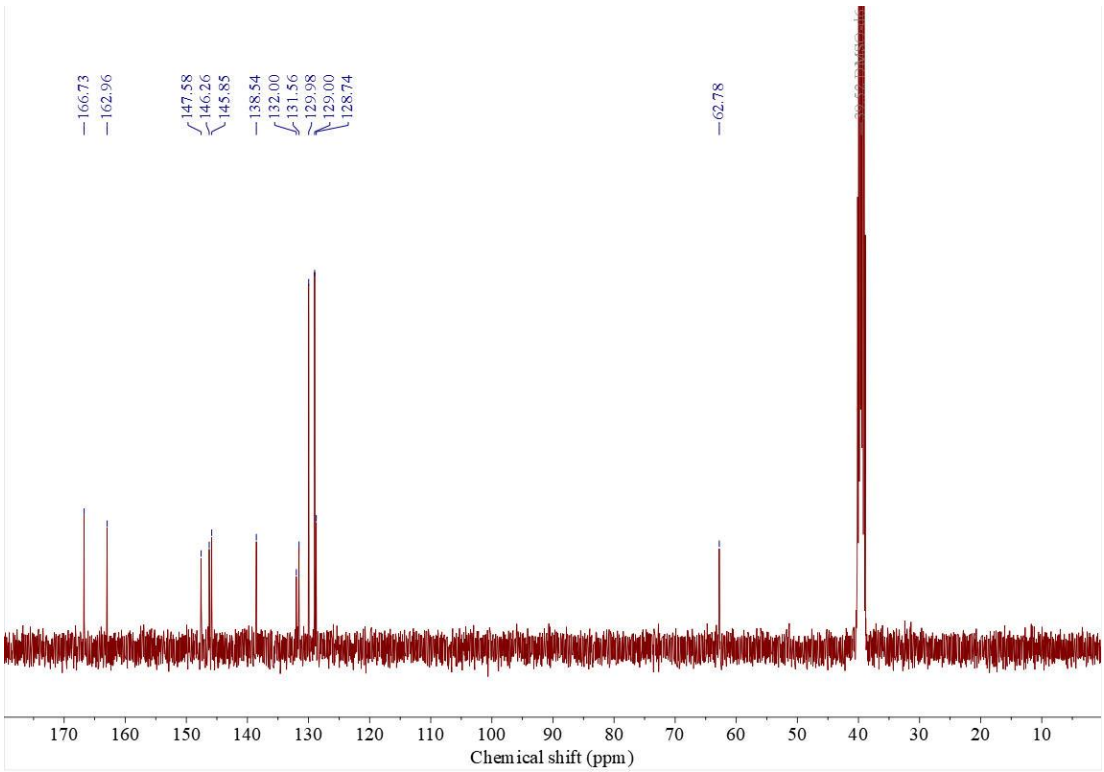

Figure S2. ^{13}C NMR spectrum of H_2**L3**.

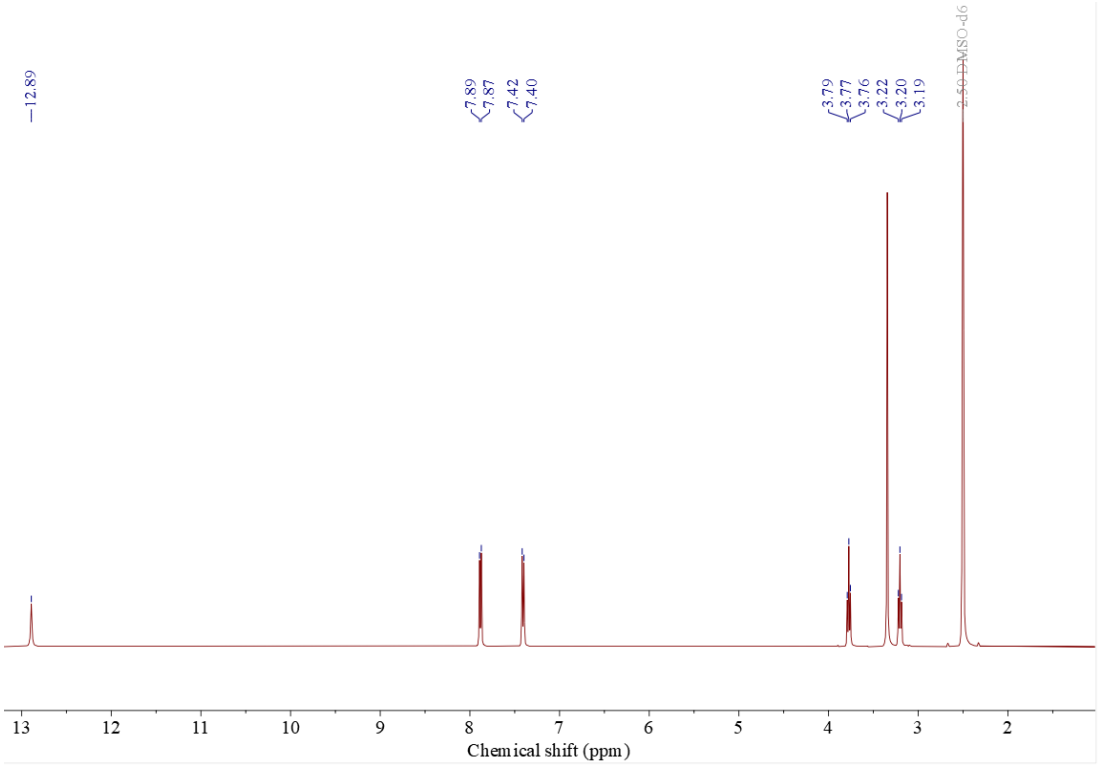

Figure S3. [1]H NMR spectrum of 4-(2-bromoethyl) benzoic acid.

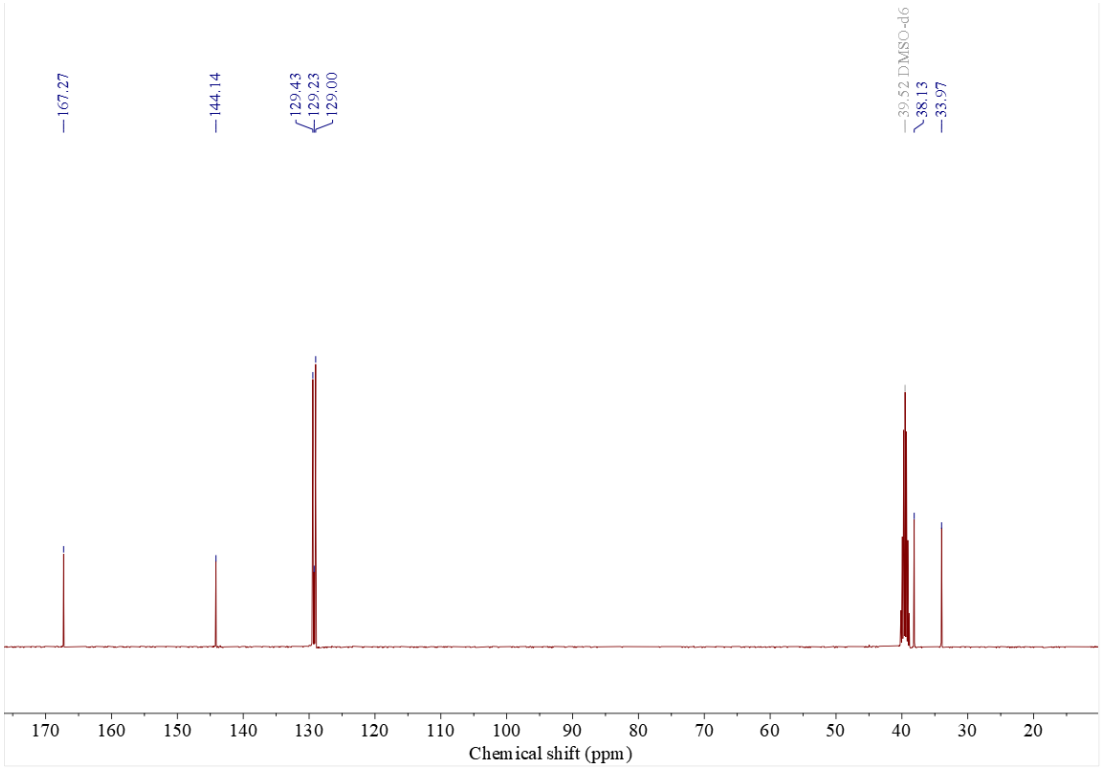

Figure S4. [13]C NMR spectrum of 4-(2-bromoethyl) benzoic acid.

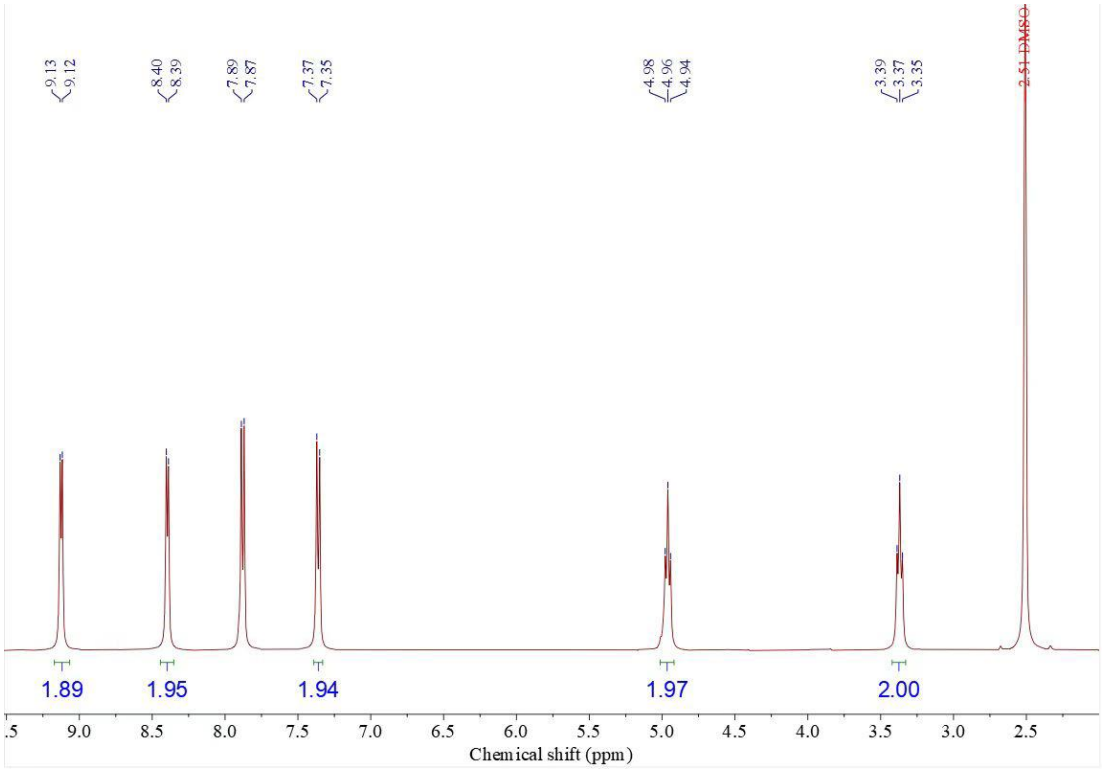

Figure S5. ^{1}H NMR spectrum of H_2**L4**.

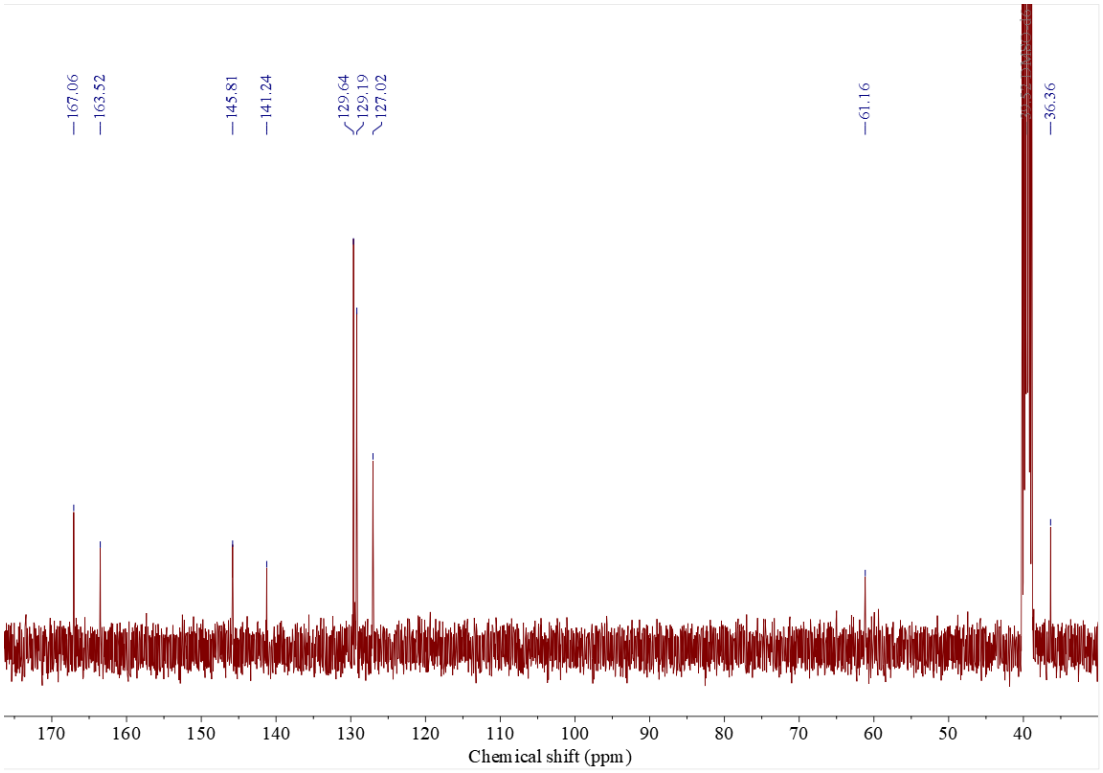

Figure S6. ^{13}C NMR spectrum of H_2**L4**.

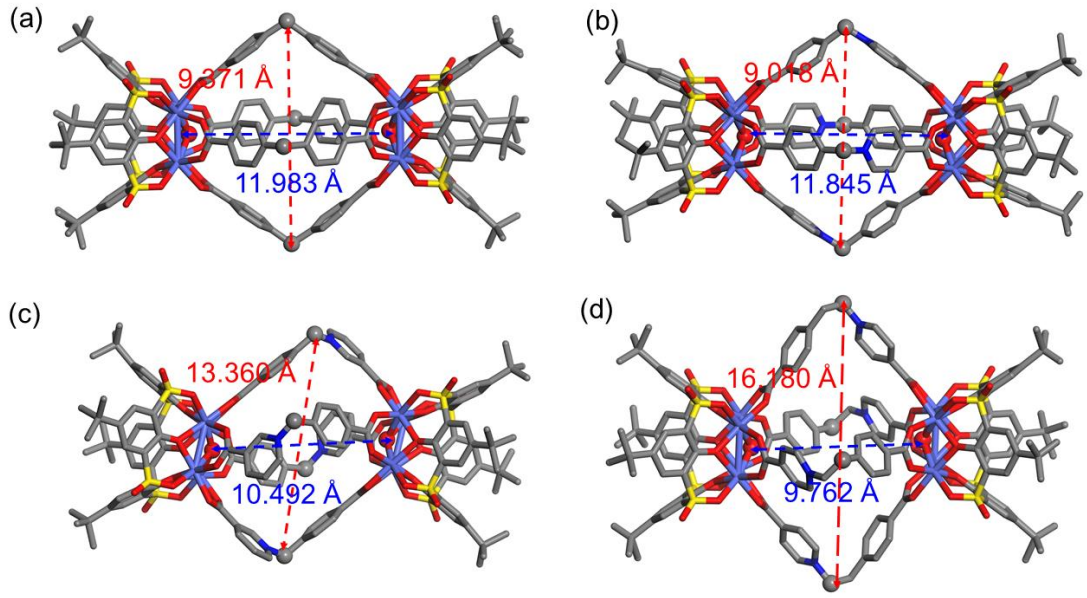

Figure S7. Crystal structures of (a) **Co-L1**, (b) **Co-L2**, (c) **Co-L3**, and (d) **Co-L4** with comparison of distances of between two μ_4-O atoms and two methylene C atoms of two opposite bridging ligands.

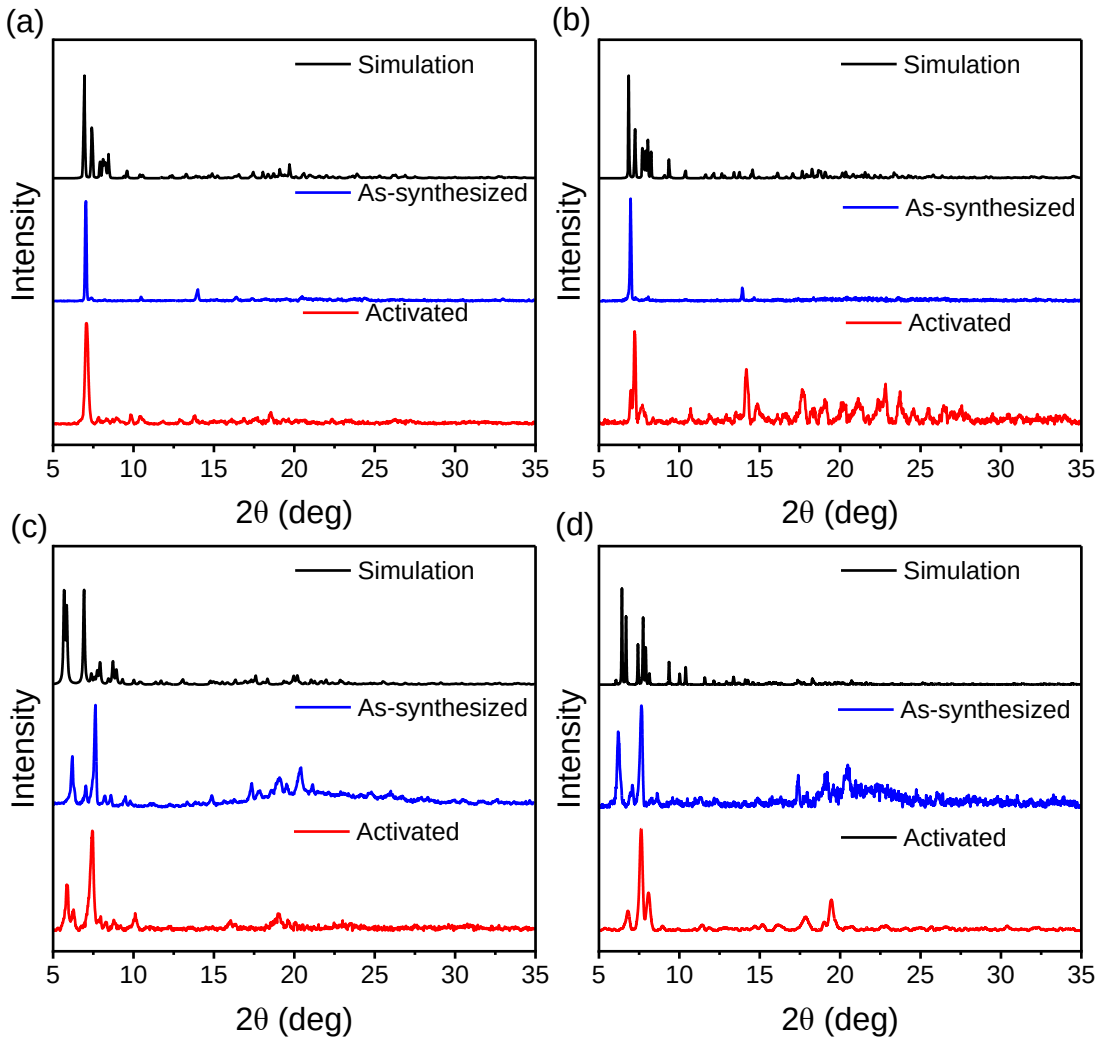

Figure S8. The experimental measured PXRD patterns of the as-synthesized and activated samples of (a) **Co-L1**, (b) **Co-L2**, (c) **Co-L3** and (d) **Co-L4**. In comparison with the simulated patterns from single-crystal structures.

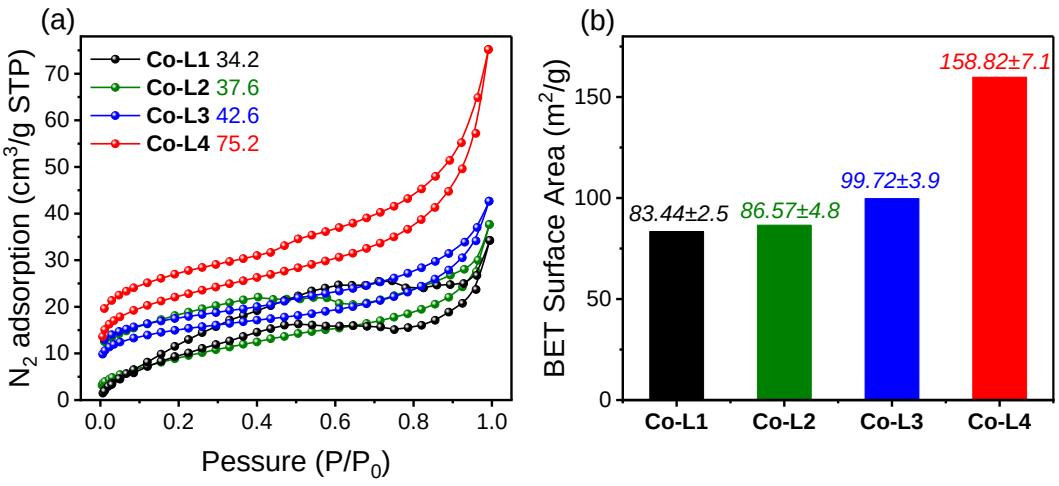

Figure S9 (a) N_2 adsorption and desorption isotherms of activated **Co-L1**, **Co-L2**, **Co-L3** and **Co-L4**; (b) BET surface areas of **Co-L1**, **Co-L2**, **Co-L3** and **Co-L4**.

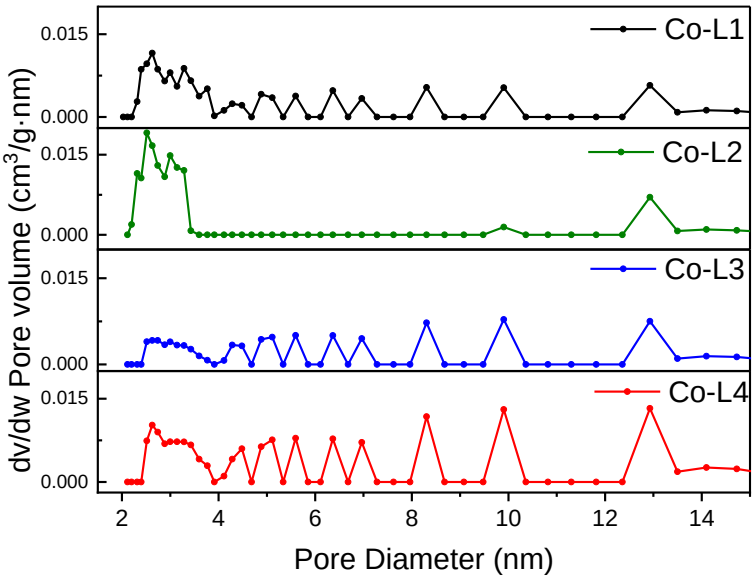

Figure S10 DFT pore size distribution curves of **Co-L1**, **Co-L2**, **Co-L3** and **Co-L4**. The pore size distribution was calculated based on the non-local density functional theory (NLDFT) using the N_2@77-Carb cylindrical pore model; the micropore volume, mesopore volume, and total pore volume were determined.

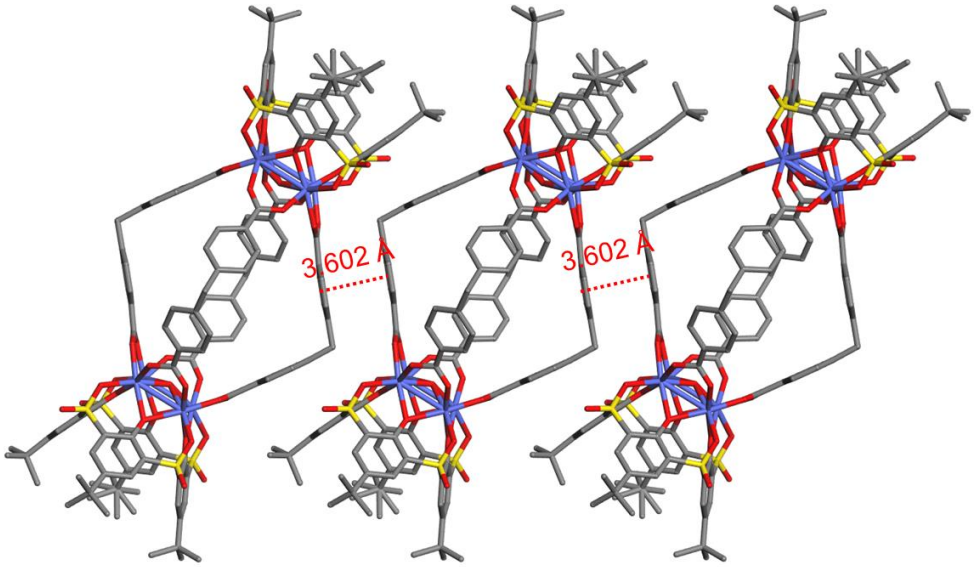

Figure S11. Molecular packing diagram and π–π stacking distance of **Co-L1**.

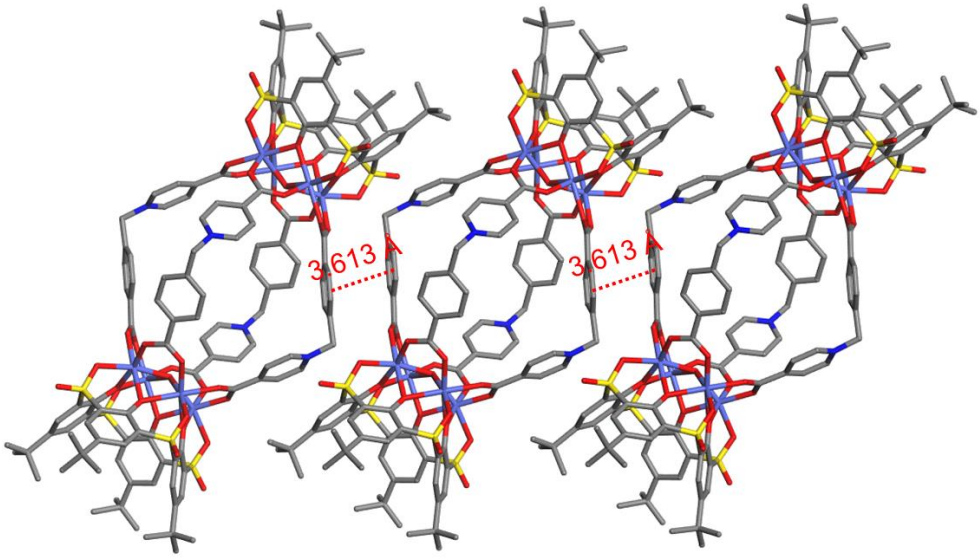

Figure S12. Molecular packing diagram and π–π stacking distance of **Co-L2**.

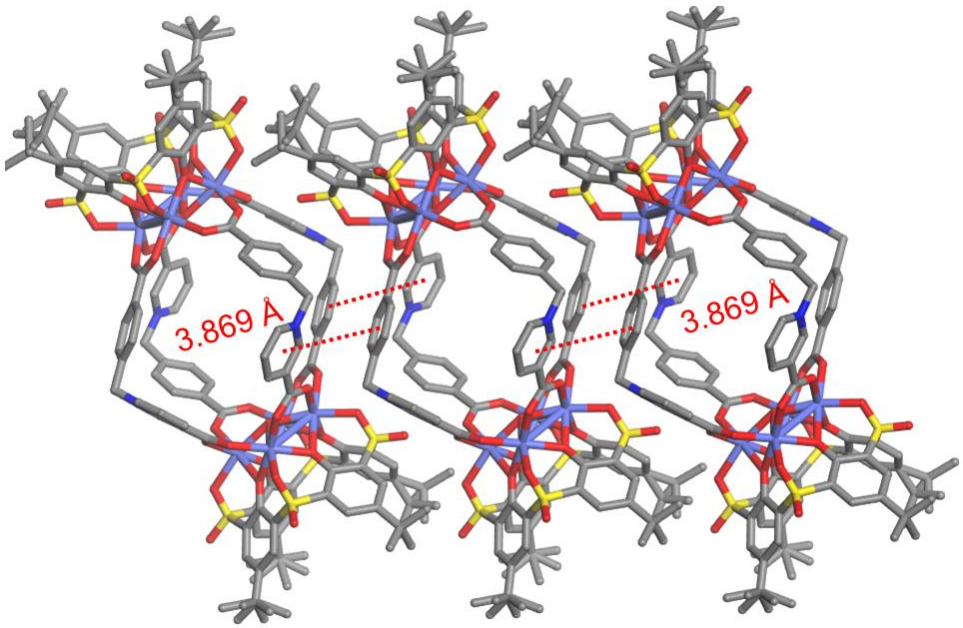

Figure S13. Molecular packing diagram and π–π stacking distance of **Co-L3**.

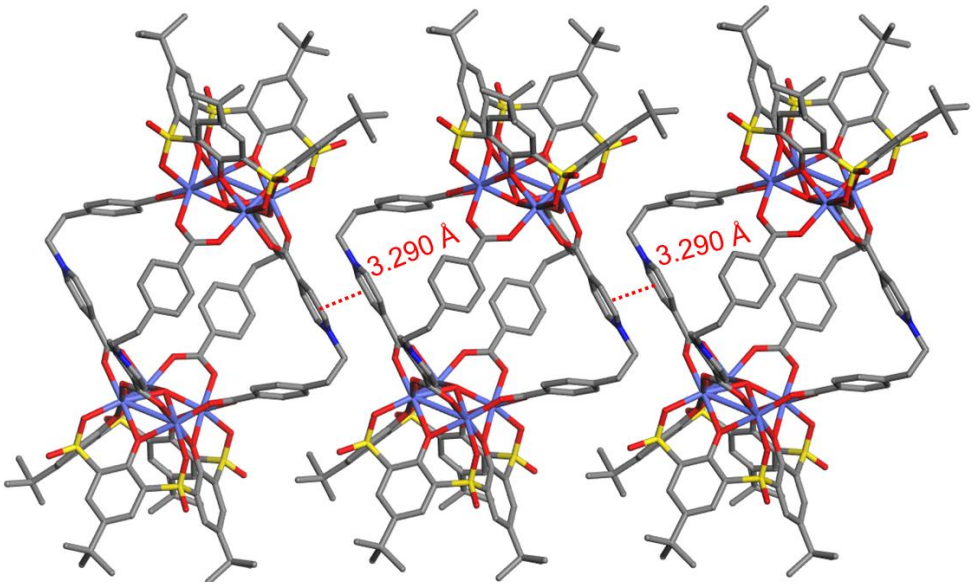

Figure S14. Molecular packing diagram and π–π stacking distance of **Co-L4**.

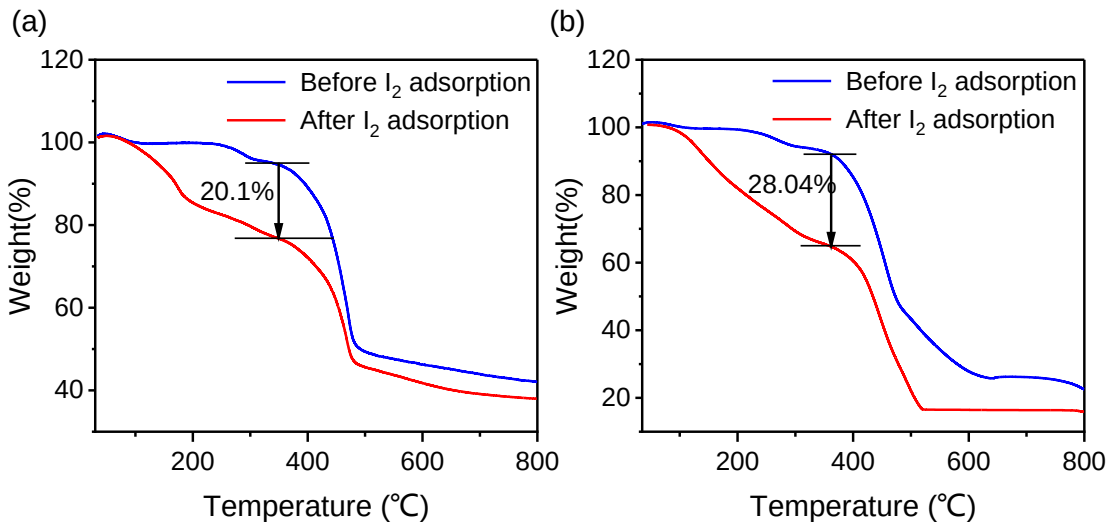

Figure S15. TGA curves of (a) **Co-L3** and (b) **Co-L4** before and after I_2 adsorption.

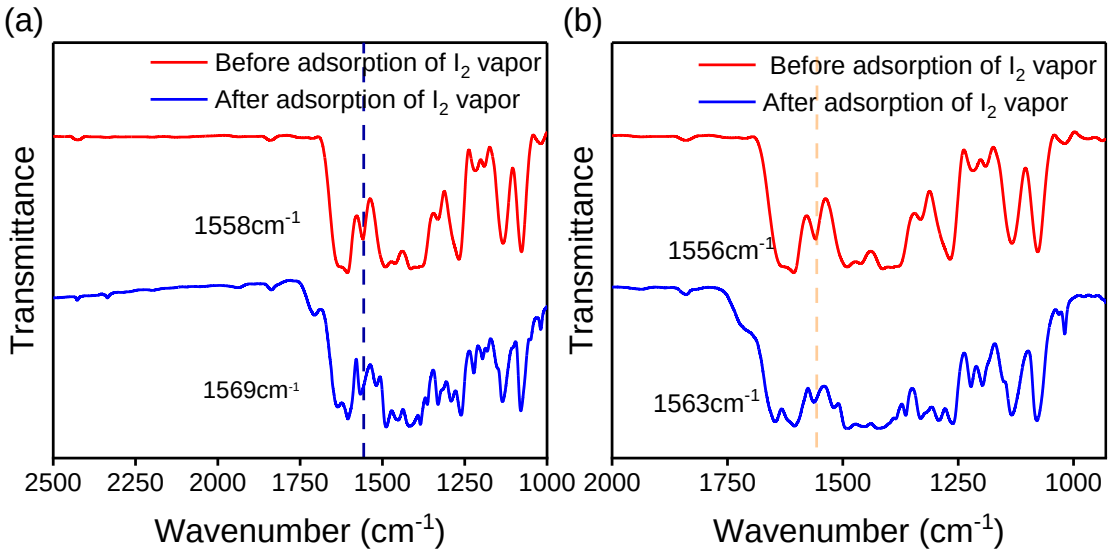

Figure S16. FT-IR spectra of (a) **Co-L3** and (b) **Co-L4** before and after I_2 adsorption.

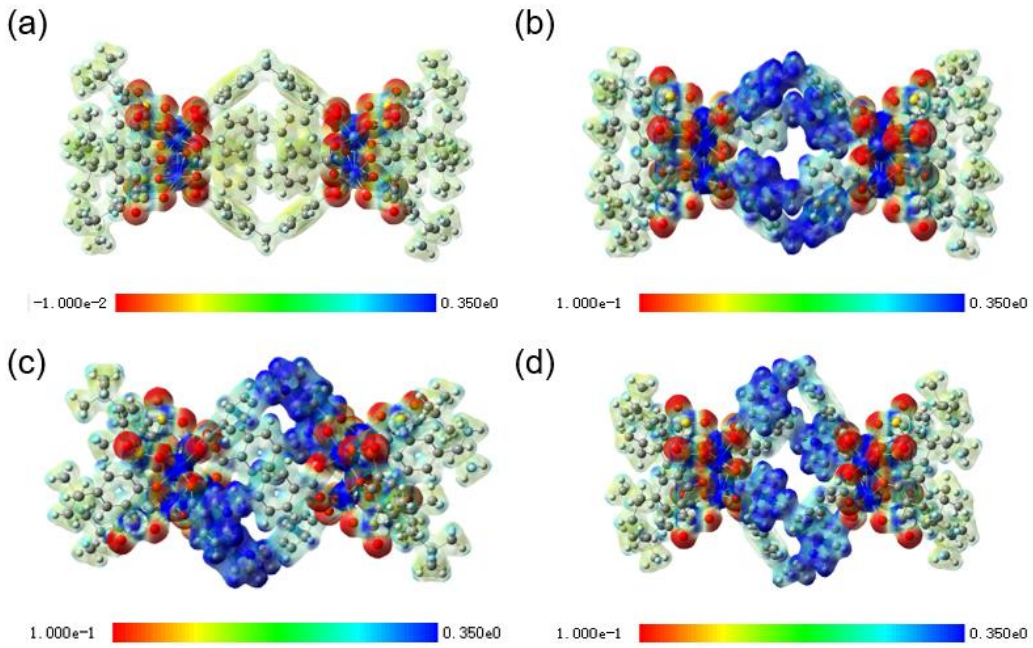

Figure S17. Molecular electrostatic potential (ESP) distributions of (a) **Co-L1**, (b) **Co-L2**, (c) **Co-L3**, and (d) **Co-L4**.

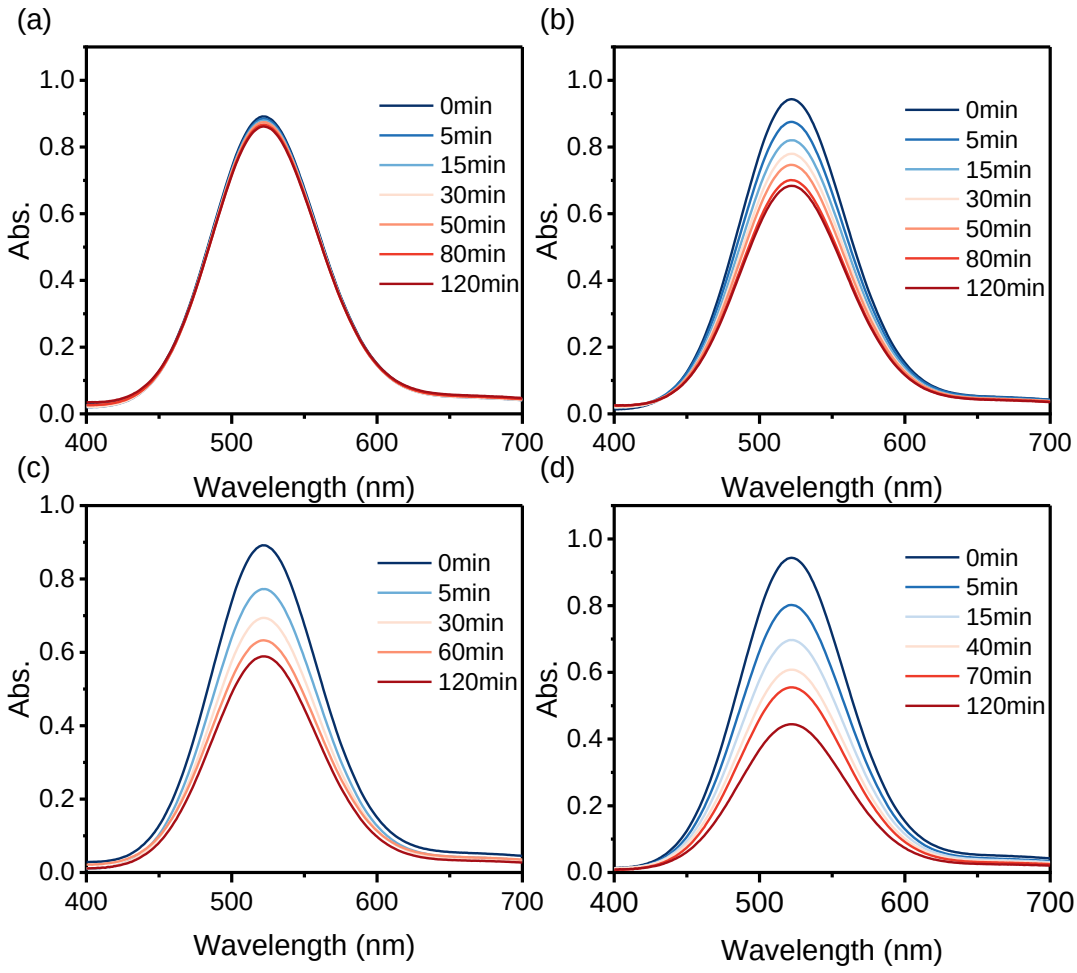

Figure S18. Time-dependent UV-Vis spectra of I_2 in n-hexane solution during the adsorption by solids of (a) **Co-L1**, (b) **Co-L2**, (c) **Co-L3**, and (d) **Co-L4**.

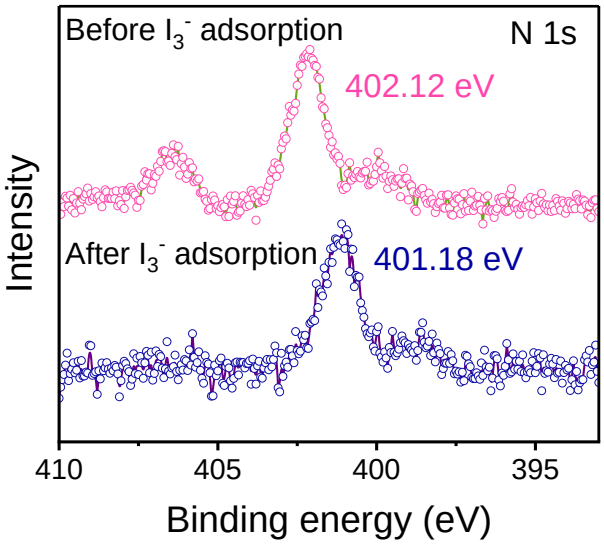

Figure S19. XPS spectra of **Co-L4** before and after I_3^- adsorption.

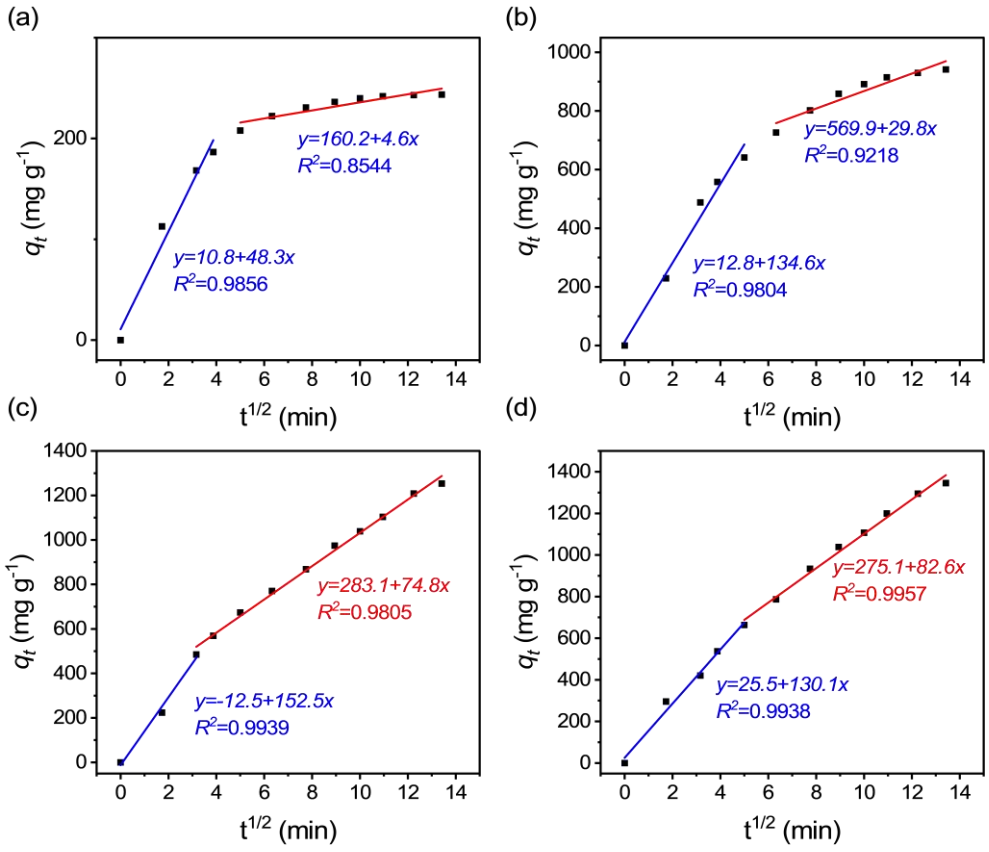

Figure S20. Weber-Morris intraparticle diffusion model of (a) **Co-L1**, (b) **Co-L2**, (c) **Co-L3**, and (d) **Co-L4**.

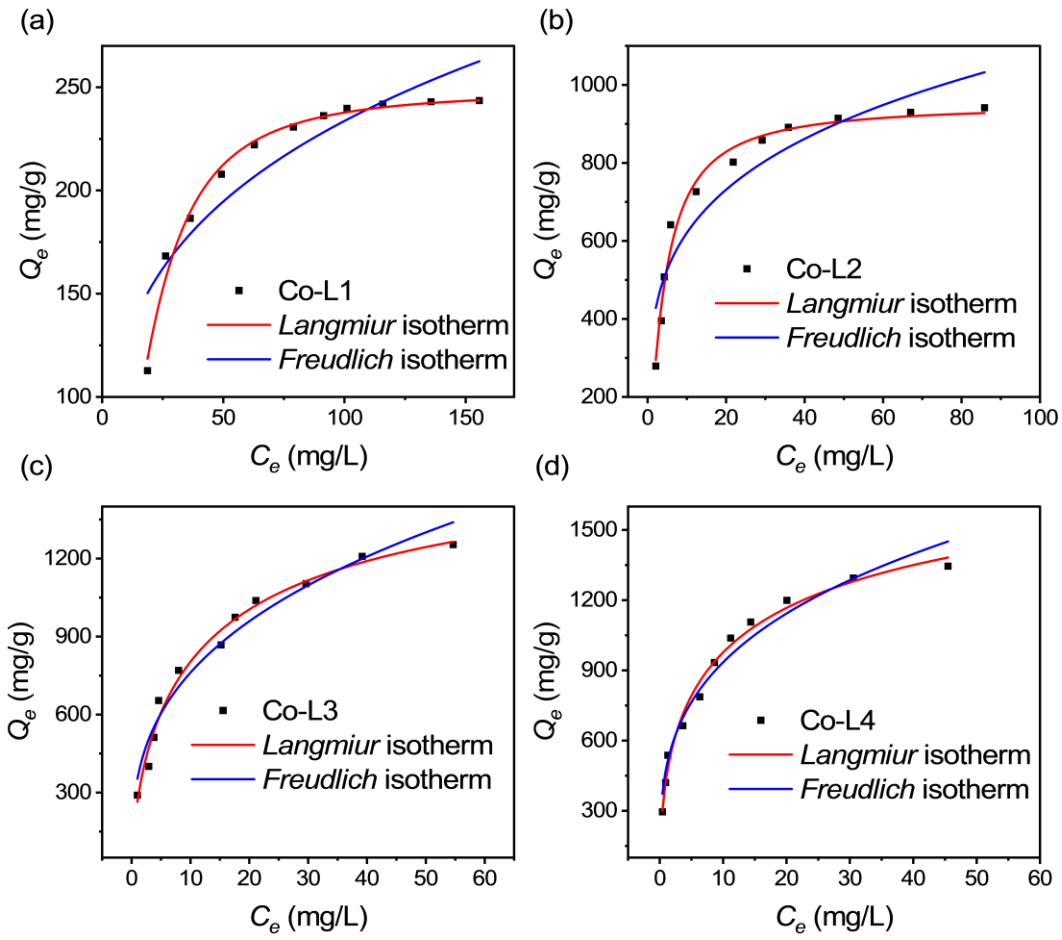

Figure S21. Langmuir and Freundlich isothermal adsorption model fitting curves of (a) **Co-L1**, (b) **Co-L2**, (c) **Co-L3**, and (d) **Co-L4**.

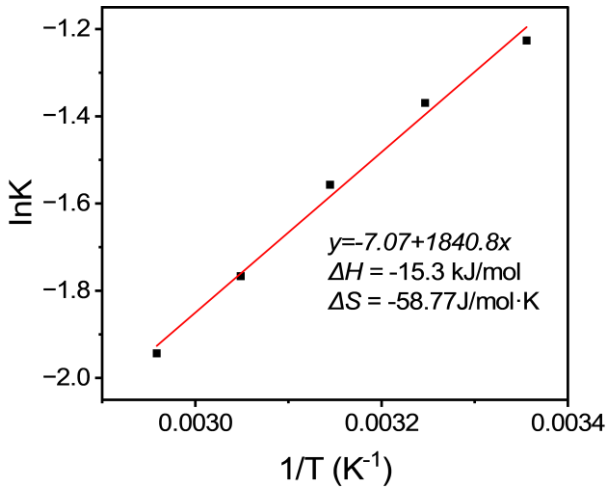

Figure S22. Van't Hoff plot for I_3^- adsorption on **Co-L4**.

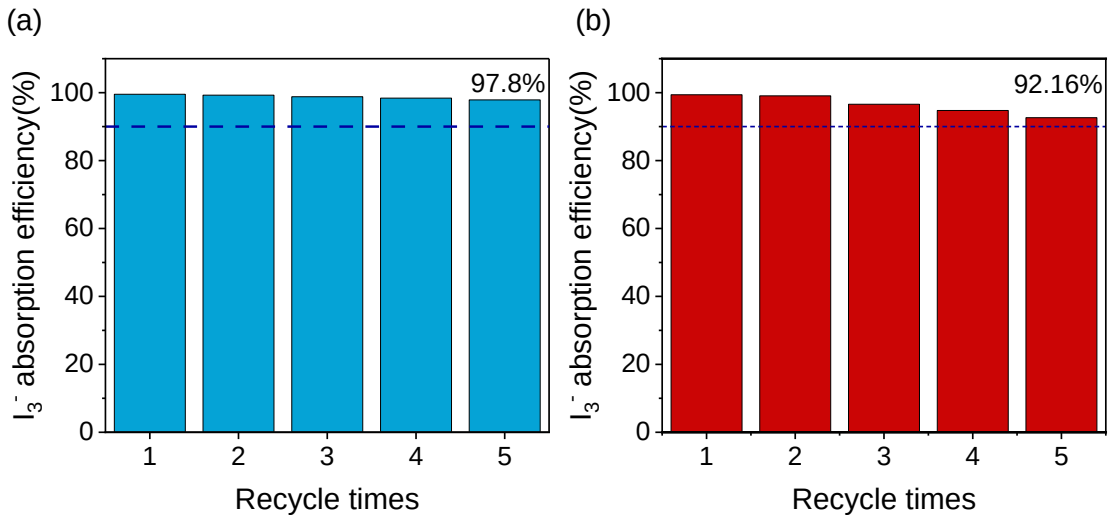

Figure S23. Cyclic adsorption performance of (a) **Co-L3** and (b) **Co-L4** toward I_3^- in aqueous solution.

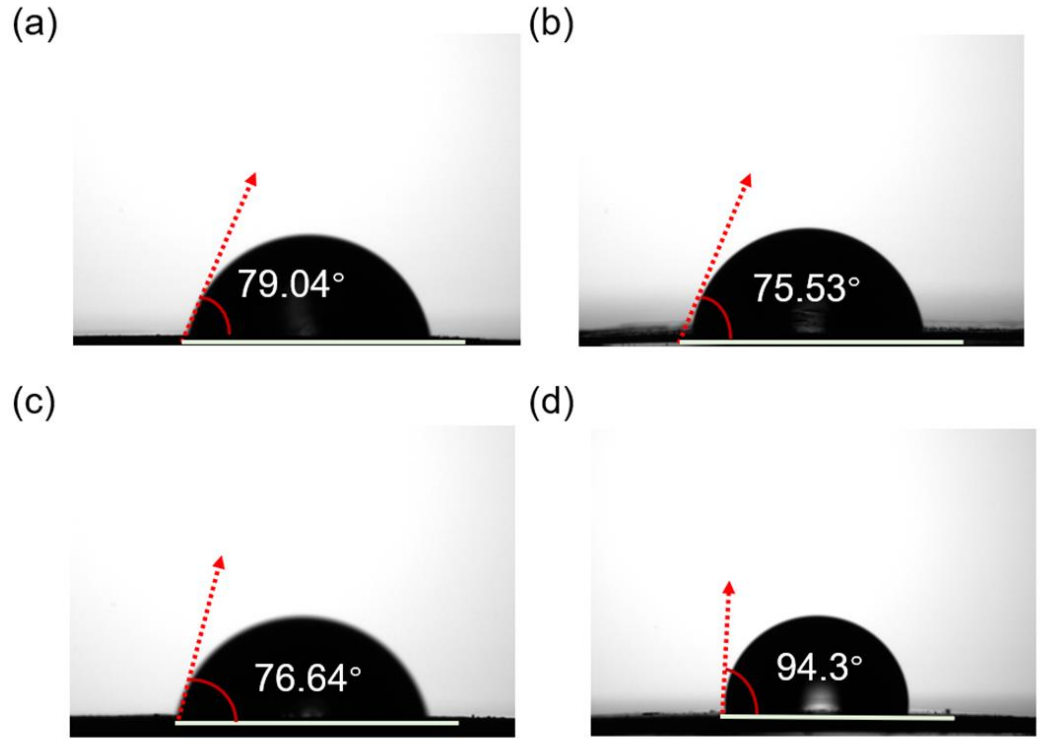

Figure S24. The water contact angle images of (a) **Co-L1**, (b) **Co-L2**, (c) **Co-L3**, and (d) **Co-L4**.

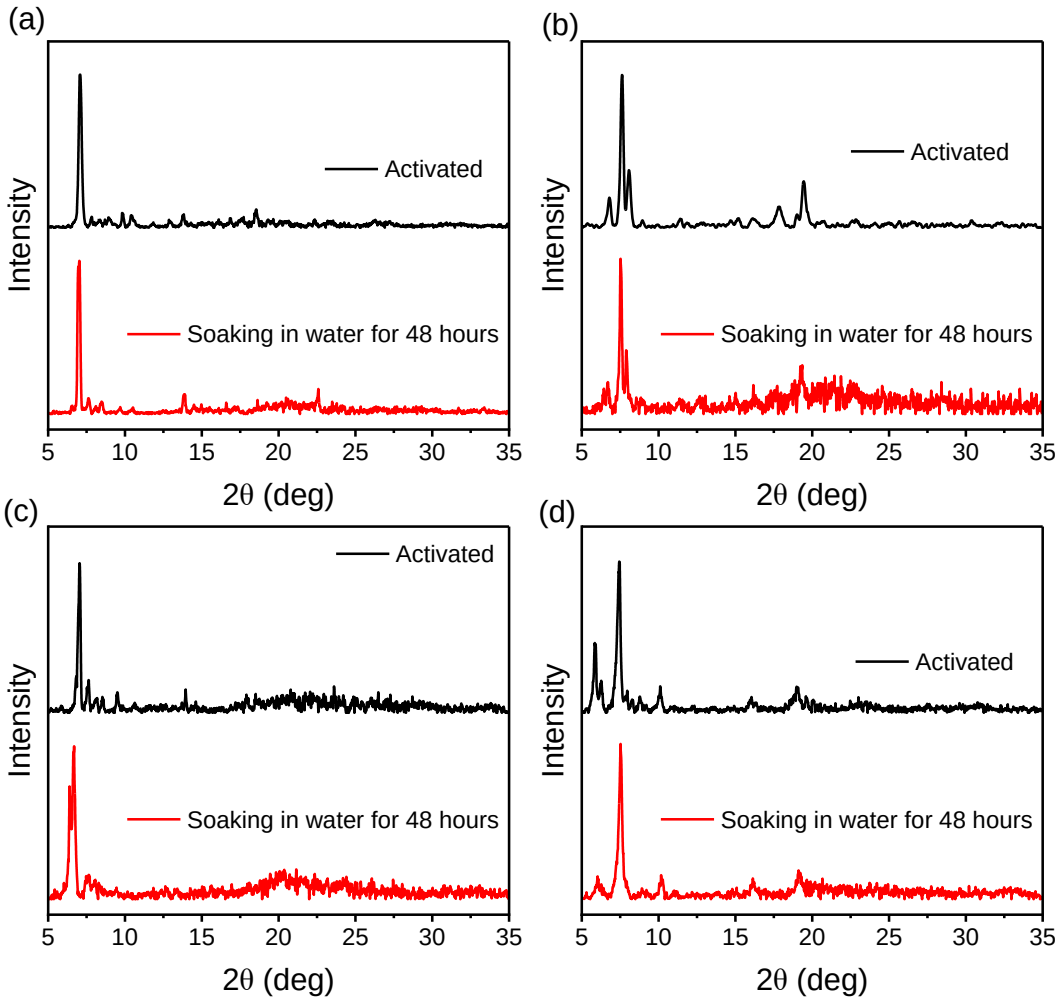

Figure S25. PXRD patterns of samples after activation and soaking in water for 48 hours (a) **Co-L1**, (b) **Co-L2**, (c) **Co-L3**, and (d) **Co-L4**.

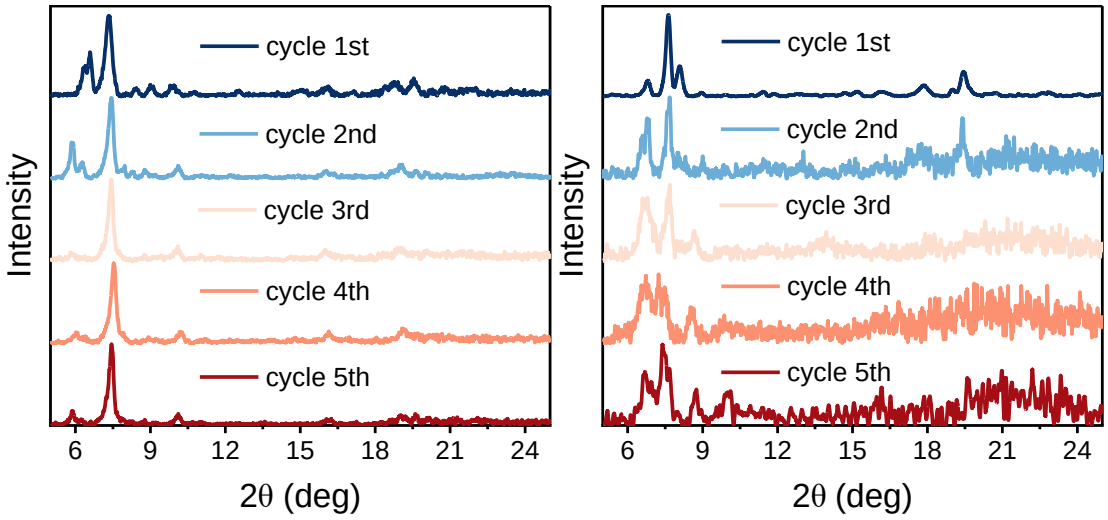

Figure S26. PXRD patterns of (a) **Co-L3** and (b) **Co-L4** during different cycle of I_3^- adsorption experiments.

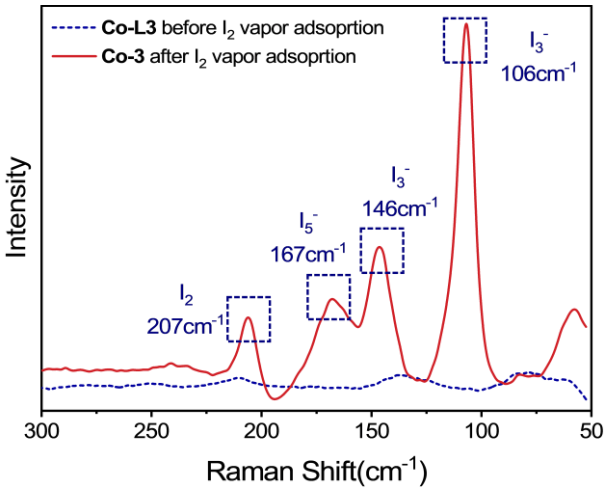

Figure S27. Raman spectrum of **Co-L3** before and after I_2 adsorption.

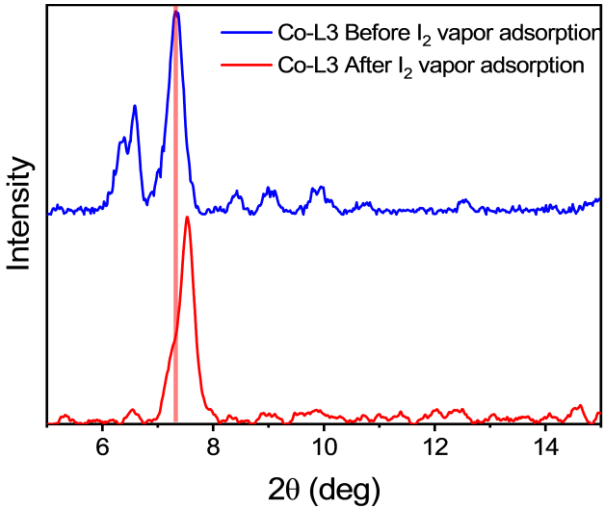

Figure S28. PXRD pattern of **Co-L3** before and after I_2 adsorption.

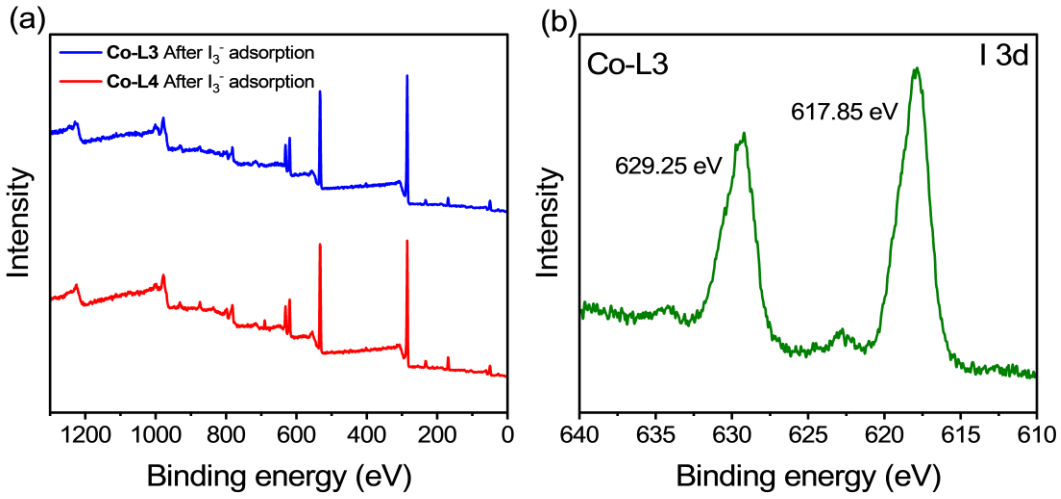

Figure S29. (a)Full XPS spectrum of **Co-L3** and **Co-L4** after I_3^- adsorption, (b) I 3d XPS spectrum of **Co-L3** after I_3^- adsorption.

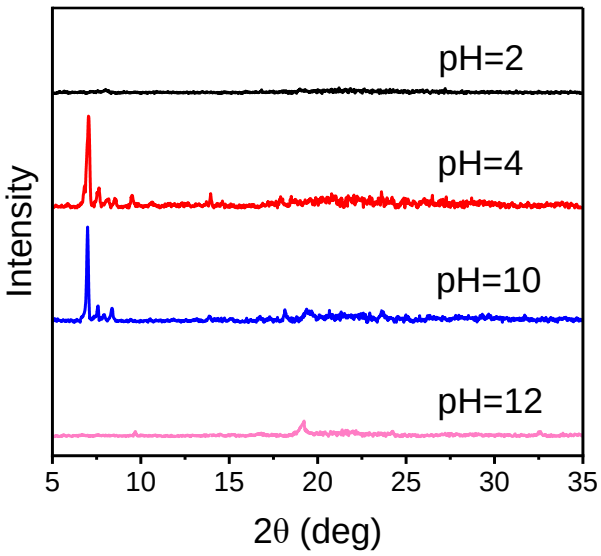

Figure S30. PXRD patterns of **Co-L2** after soaking in aqueous solutions with different pH values.

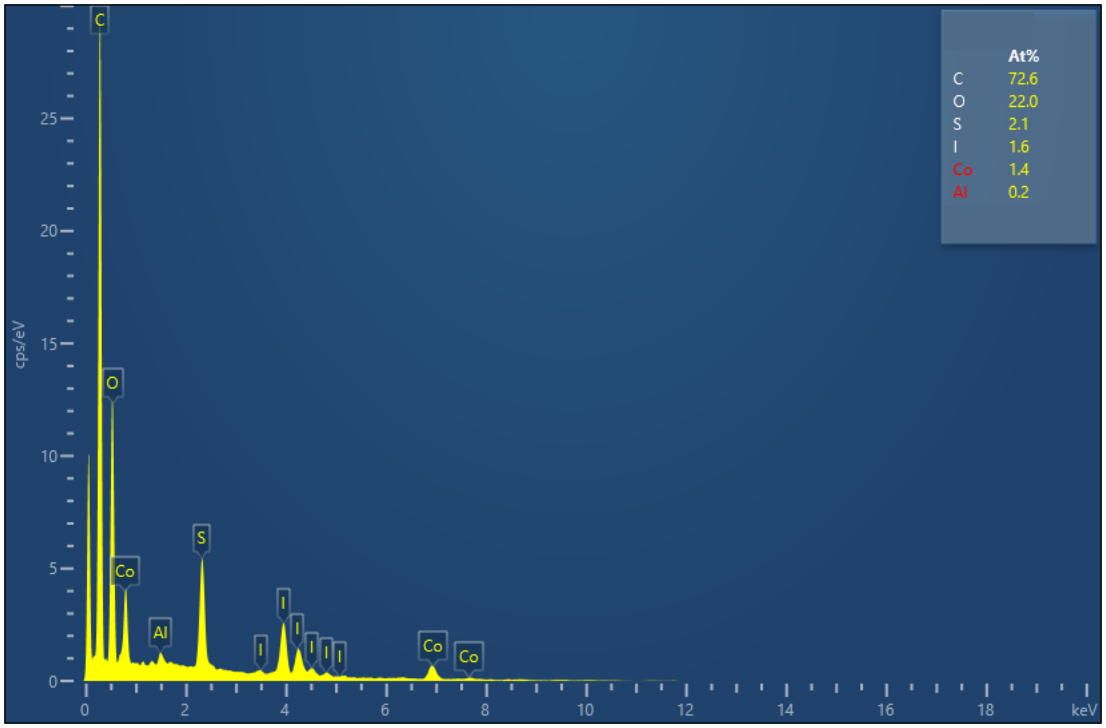

Figure S31. EDS spectrum of **Co-L3** after I_3^- adsorption.

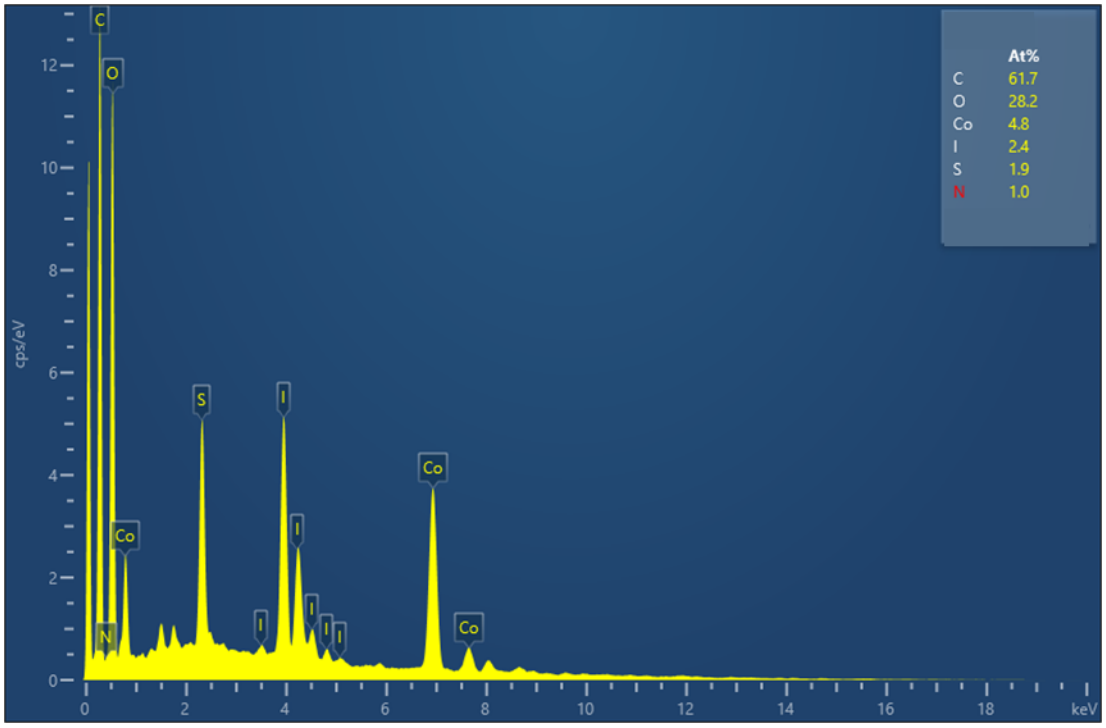

Figure S32. EDS spectrum of **Co-L4** after I_3^- adsorption.

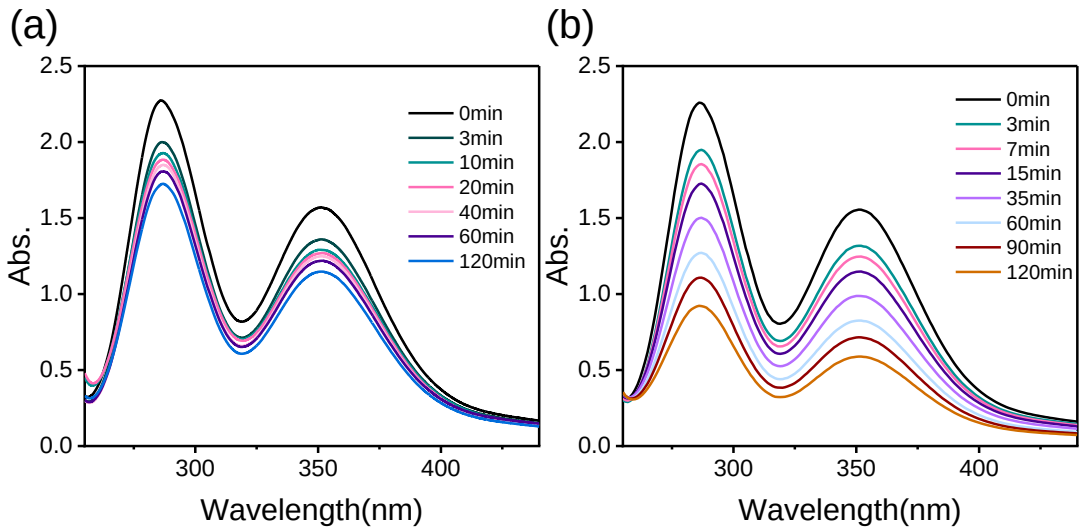

Figure S33. Time-dependent UV-Vis spectra of I_3^- in aqueous solution during the adsorption by solids of (a) **Co-L1** and (b) **Co-L2**.

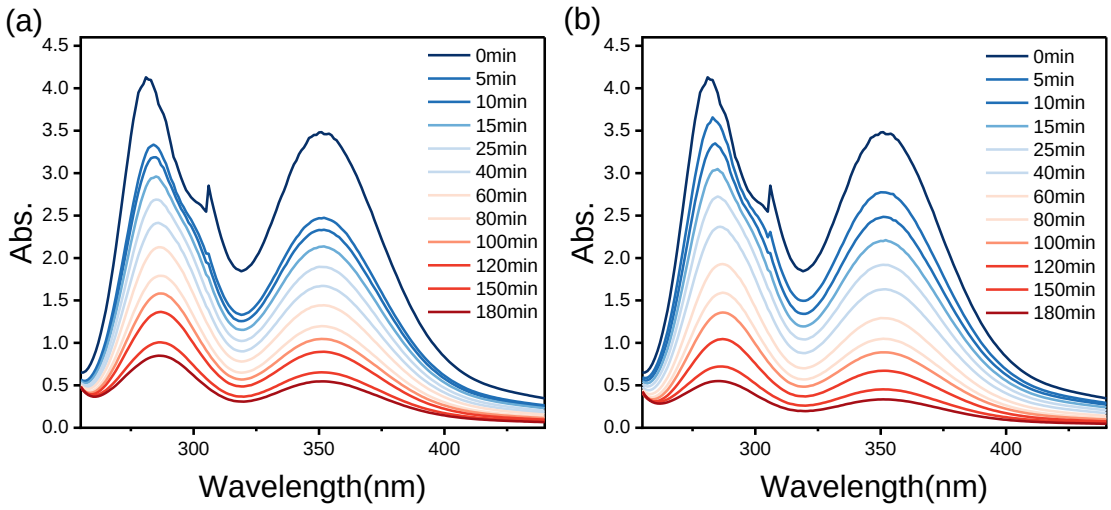

Figure S34. Time-dependent UV-Vis spectra of I_3^- in aqueous solution during the adsorption by solids of (a) **Co-L3** and (b) **Co-L4**.

References

[1] Gaussian 16, Revision C.01, M. J. Frisch, G. W. Trucks, H. B. Schlegel, G. E. Scuseria, M. A. Robb, J. R. Cheeseman, G. Scalmani, V. Barone, G. A. Petersson, H. Nakatsuji, X. Li, M. Caricato, A. V. Marenich, J. Bloino, B. G. Janesko, R. Gomperts, B. Mennucci, H. P. Hratchian, J. V. Ortiz, A. F. Izmaylov, J. L. Sonnenberg, D. Williams-Young, F. Ding, F. Lipparini, F. Egidi, J. Goings, B. Peng, A. Petrone, T. Henderson, D. Ranasinghe, V. G. Zakrzewski, J. Gao, N. Rega, G. Zheng, W. Liang, M. Hada, M. Ehara, K. Toyota, R. Fukuda, J. Hasegawa, M. Ishida, T. Nakajima, Y. Honda, O. Kitao, H. Nakai, T. Vreven, K. Throssell, J. A. Montgomery, Jr., J. E. Peralta, F. Ogliaro, M. J. Bearpark, J. J. Heyd, E. N. Brothers, K. N. Kudin, V. N. Staroverov, T. A. Keith, R. Kobayashi, J. Normand, K. Raghavachari, A. P. Rendell, J. C. Burant, S. S. Iyengar, J. Tomasi, M. Cossi, J. M. Millam, M. Klene, C. Adamo, R. Cammi, J. W. Ochterski, R. L. Martin, K. Morokuma, O. Farkas, J. B. Foresman, and D. J. Fox, Gaussian, Inc., Wallingford CT, **2016**.

[2] C. T. Lee, W. T. Yang and R. G. Parr, Development of the Colle-Salvetti correlation-energy formula into a functional of the electron density, *Phys. Rev. B*, 1988, **37**, 785-789.

[3] A. D. Becke, Density-functional exchange-energy approximation with correct asymptotic behavior, *Phys. Rev. A*, 1988, **38**, 3098-3100.

[4] S. Grimme, J. Antony, S. Ehrlich and H. Krieg, H. A consistent and accurate ab initio parameterization of density functional dispersion correction (DFT-D) for the 94 elements H-Pu, *J. Chem. Phys.*, 2010, **132**, 154104.

[5] D. Andrae, U. Häussermann, M. Dolg, H. Stoll and H. Preuss, Energy-adjusted ab initio pseudopotentials for the second and third row transition elements, *Theor. Chim. Acta*, 1990, **77**, 123-141.

[6] M. P. Moloney, N. Massoni, S. Egodawatte, H.-C. zur Loye and A. Grandjean, A Solvent Free Approach for the Preparation of Silver Modified Mesoporous Silica for Iodine Entrapment, *J. Inorg. Organomet. Polym. Mater.*, 2020, **30**, 2756-2763.

[7] X. Yuan, W. Yu, X. Xiao, L. Wang and Q. Wan, Removal of iodide from aqueous solutions using a silver-modified ZnAl layered double hydroxide, *J. Solid State Chem.*, 2024, **335**, 124731.

[8] M. Jiang, T. Tian, J. Yang, T. Chang, J. Peng, H. Shi, Z. Ahmad, Z. Zhu, X. Du, H Zhang, et al., Nitrogen-rich mesoporous silica foam for efficient radioactive iodine capture from vapor and aqueous phases, *J. Environ. Chem. Eng.*, 2025, **13**, 118944.

[9] Y.-H. Wang, Y.-Q. Xiang, R.-X. Hu, S. Qin, G.-H. Tao and L. He, Hydrophobic ionic microspheres based on multiple hydrogen bonding for iodine capture in humid environments, *Chem. Eng. J.*, 2025, **524**, 169287.

[10] T. Pan, X. Dong and Y. Han, Efficient capture of iodine and methyl iodide using all-silica EMM-17 zeolite, *Nano Res.*, 2023, **16**, 6308–6315.

[11] Q. Zhao, C. Liao, G. Chen, R. Liu, Z. Wang, A. Xu, S. Ji, K. Shih, L. Zhu and T. Duan, In Situ Confined Synthesis of a Copper-Encapsulated Silicalite-1 Zeolite for Highly Efficient Iodine Capture, *Inorg. Chem.*, 2022, **61**, 20133–20143.

[12] X. Wang, J. Bian, J. Yang, M. She, H. Jin, W. Liu and W. Liu, Functional-Oriented Strategy Construction of Hydrogen-Bonded Organic Porous Polymers for Efficient Capture of Radioactive Iodine in the Environment, *ACS Appl. Eng. Mater.*, 2025, **3**, 4449–4457.

[13] H. Li, Y. Li, B. Li, D. Liu and Y. Zhou, Highly selective anchoring silver nanoclusters on MOF/SOF heterostructured framework for efficient adsorption of radioactive iodine from aqueous solution, *Chemosphere*, 2020, **252**, 126448.

[14] T. He, X. Xu, B. Ni, H. Lin, C. Li, W. Hu and X. Wang, Metal-Organic Framework Based Microcapsules, *Angew. Chem., Int. Ed.*, 2018, **57**, 10148–10152.

[15] X. Li, Y. Wang, T. Li, J. Zhang, Y. Shen, X. Qu, Y. Yang and X. Yu, Efficient and Selective Removal of Iodine in Aqueous Media Using Morphology-Controlled Porous Hyper-Cross-Linked Polymers, *ACS Appl. Polym. Mater.*, 2025, **7**, 1639–1650.

[16] A. Sen, S. Sharma, S. Dutta, M. M. Shirolkar, G. K. Dam, S. Let and S. K. Ghosh, Functionalized Ionic Porous Organic Polymers Exhibiting High Iodine Uptake from Both the Vapor and Aqueous Medium, *ACS Appl. Mater. Interfaces*, 2021, **13**, 34188–34196.

[17] Y. Chen, M.-K. Yang, S.-X. Li, S.-L. Zhou, C.-N. Hu, Y.-H. Yang and L.-J. Yang, Imidazole Cationic-Bridged Pillar[5]arene Polymer as a Recycle Adsorbent for Iodine Capture, *ACS Appl. Mater. Interfaces*, 2025, **17**, 8382–8393.

[18] L. Li, G. Yang and Y. Wang, Efficient iodine adsorption from water using tailored multi-heteroatom porous metal-organic framework by dual-ligand strategy, *Sep. Purif. Technol.*, 2025, **370**, 133227.

[19] M. Zhu, S. Wang, A. Zhang, C. Sun, K. Huang, Y. Lu, Y. Liu and S. Liu, Construction of Unsaturated Coordinated Cu-Metal-Organic Frameworks for Iodine Adsorption, *Inorg. Chem.*, 2026, **65**, 913–919.

[20] A.-M. Song, F.-D. Zhang, Z.-H. Peng, R.-P. Liang, J.-Z. Liao, H. Ke, L. Zhang and J.-D. Qiu, Precise Identification of Radioactive Iodine within Interlayer Molecular Cages of Metal–Organic Frameworks, *J. Am. Chem. Soc.*, 2025, **147**, 32352–32356.

[21] M. Dalapati, R. Singha, P. Maity, D. Manna and D. Samanta, Self-Assembled Pd(II) Nano-Adsorbents for Iodine and Methyl Iodide Capture in Vapor and Aqueous Phases, *Small*, 2025, **21**, 2504242.

[22] R. Guan, J. D. Jensen, S. Liang, G. Li, Y. Liu, R. Lavendomme, B. W. Laursen, E.-Q. Gao and D. Zhang, Integrating Photoredox and Anion-Binding Capabilities into a Metal-Organic Cage for Iodine Speciation and Sequestration, *Aggregate*, 2025, e70203.

[23] A. Gogia, H. Bhambri and S. K. Mandal, Exploiting a Multi-Responsive Oxadiazole Moiety in One Three-Dimensional Metal-Organic Framework for Remedies to Three Environmental Issues, *ACS Appl. Mater. Interfaces*, 2023, **15**, 8241–8252.

[24] Y. Han, Y. He, Y.-K. Fu, et al., Crystallographic Visualization of Distinct Iodic Aggregations in Isostructural Metal-Organic Frameworks, *J. Am. Chem. Soc.*, 2025, **147**, 19968–19975.

[25] R. Liu, W. Zhang, Y. Chen, C. Xu, G. Hu and Z. Han, Highly efficient adsorption of iodine under ultrahigh pressure from aqueous solution, *Sep. Purif. Technol.*, 2020, **233**, 115999.

[26] A. Gogia, P. Das and S. K. Mandal, Tunable Strategies Involving Flexibility and Angularity of Dual Linkers for a 3D Metal-Organic Framework Capable of Multimedia Iodine Capture, *ACS Appl. Mater. Interfaces*, 2020, **12**, 46107–46118.

[27] Y. Wang, Y. Chen, M. Zhao, L. Zhang, C. Zhou and H. Wang, *Environ.* Simulated adsorption of iodine by an amino-metal-organic framework modified with covalent bonds, *Sci. Pollut. Res.*, 2022, **29**, 88882–88893.

[28] J. Qin, W. Zhang, Y. Chen, R. Liu and Y. Fan, *Environ.* Zinc-based triazole metal complexes for efficient iodine adsorption in water, *Sci. Pollut. Res.*, 2021, **28**, 28797–28807.

[29] L. Yang, C. Zhao, W. Ma, X. Huang, H. Zhang, P. Zhang and Y. Ke, Ionic post-synthetic functionalization of acylhydrazone-linked COFs for tailored and enhanced iodine adsorption, *Sep. Purif. Technol.*, 2026, **393**, 137273.

[30] Y. Lin, X. Jiang, S. T. Kim, S. B. Alahakoon, X. Hou, Z. Zhang, C. M. Thompson, R. A. Smaldone and C. Ke, An Elastic Hydrogen-Bonded Cross-Linked Organic Framework for Effective Iodine Capture in Water, *J. Am. Chem. Soc.*, 2017, **139**, 7172–7175.

[31] M. Zhang, J. Samanta, B. A. Atterberry, R. Staples, A. J. Rossini and C. Ke, A Crosslinked Ionic Organic Framework for Efficient Iodine and Iodide Remediation in Water, *Angew. Chem., Int. Ed.*, 2022, **61**, e202214189.

[32] H. J. Choi and M. P. Suh, Dynamic and Redox Active Pillared Bilayer Open Framework: Single-Crystal-to-Single-Crystal Transformations upon Guest Removal, Guest Exchange, and Framework Oxidation, *J. Am. Chem. Soc.*, 2004, **126**, 15844–15851.

[33] Y. Wang, Y. Jin, W. Xian, X. Zuo, S. Wang and Q. Sun, Pore polarity engineering in hydrogen-bonded organic frameworks for enhanced iodine capture, *J. Mater. Chem. A*, 2022, **10**, 18730–18736.

[34] R. Chen, T. Hu and Y. Li, Stable nitrogen-containing covalent organic framework as porous adsorbent for effective iodine capture from water, *React. Funct. Polym.*, 2021, **159**, 104806.

[35] D. Li, G. Wu, Y.-K. Zhu and Y.-W. Yang, Phenyl-Extended Resorcin[4]arenes: Synthesis and Highly Efficient Iodine Adsorption, *Angew. Chem., Int. Ed.*, 2024, **63**, e202411261.

[36] Y. Liao, J. Li and A. Thomas, General Route to High Surface Area Covalent Organic Frameworks and Their Metal Oxide Composites as Magnetically Recoverable Adsorbents and for Energy Storage, *ACS Macro Lett.*, 2017, **6**, 1444–1450.

[37] G. Matthys, A. Laemont, N. De Geyter, R. Morent, R. Lavendomme and P. Van Der Voort, Robust Imidazopyridinium Covalent Organic Framework as Efficient Iodine Capturing Materials in Gaseous and Aqueous Environment, *Small*, 2024, **20**, 2404994.

[38] J. Yang, S.-J. Hu, L.-X. Cai, L.-P. Zhou and Q.-F. Sun, Counteranion-mediated efficient iodine capture in a hexacationic imidazolium organic cage enabled by multiple non-covalent interactions, *Nat. Commun.*, 2023, **14**, 6082.

[39] M.-Y. Zhou, Z.-S. Yu, W. Deng, H.-L. Lu, X.-F. Niu, J. Tong, S.-Y. Yu and M. Fujita, $[M_8L_4]^{8+}$-Type Squares Self-Assembled by Dipalladium Corners and Bridging Aromatic Dipyrazole Ligands for Iodine Capture, *Inorg. Chem.*, 2023, **62**, 10193–10202.

[40] Z. Zeng, C. Lou, L. Hu, et al., Metal-organic cages for efficient capture and convenient detection of iodine from vapor and aqueous solutions, *Chem. Eng. J.*, 2024, **496**, 154091.

[41] L.-H. Wu, S.-N. Liu, B.-X. Zhou, S.-L. Cai, W.-G. Zhang and S.-R. Zheng, Encapsulation of a metal–organic cage-based porous salt in silica nanopores, *Chem. Commun.*, 2023, **59**, 9118–9121.

[42] W.-Q. Xu, Y.-H. Li, H.-P. Wang, J.-J. Jiang, D. Fenske and C.-Y. Su, Face-Capped M^4L_4 Tetrahedral Metal–Organic Cage: Iodine Capture and Release, Ion Exchange, and Electrical Conductivity, *Chem. Asian J.*, 2016, **11**, 216–220.